

Figure 1. (a) classification of reflections. (b),(d),(f) rendered images of *ipswich-pine-221* (specular), *orange-paint* (diffuse) and *blue-fabric* (retro-reflective). (c),(e),(g) 3-d plots of  $(l^T v, n^T l, I)$  which are projected onto the  $l^T v - n^T l$  space.

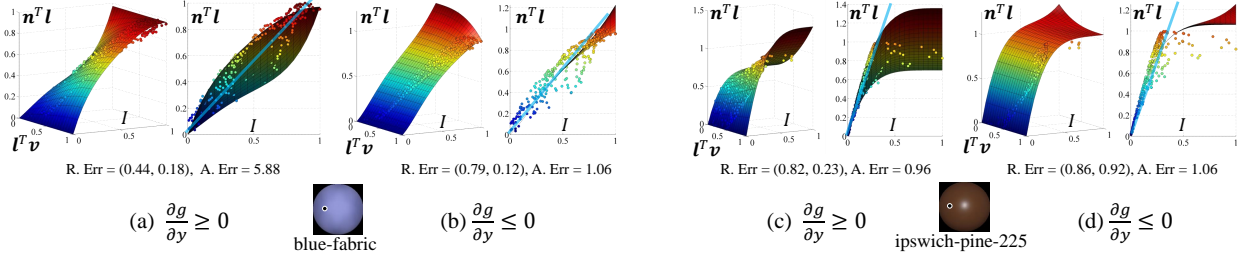


Figure 2. Illustration of regression results of the problem in Eq. (15) of our submission under (a)  $\partial g/\partial y \geq 0$  and (b)  $(\partial g/\partial y \leq 0)$  using *blue-fabric*, and (c)  $\partial g/\partial y \geq 0$  and (d)  $(\partial g/\partial y \leq 0)$  using *ipswich-pine-225*. Each 3-d plot  $(I, l^T v, n^T l)$  which were generated using recovered surface normal is overlaid with the reconstructed inverse bivariate reflectance function. At the second plots for each condition, we also overlaid the linear function fitted to recovered plots via a least-square regression. In addition, we show regression errors (R. Err) from Eq. (15) and Eq. (17) of our submission respectively with an angular error of recovered surface normal (A. Err).

## 2. Appendix B: Further Discussion about Retro-Reflective Detection in Sec. 3

This appendix provides a justification of our retro-reflective detection algorithm which was presented in Sec. 3 of our submission.

### 2.1. Why retro-reflective behavior is problematic for the inverse bivariate reflectance model?

As mentioned in Sec. 3 of our submission, our inverse bivariate reflectance model (Eq. (6) of our submission) which is derived from the sum-of-lobe representation of general isotropic BRDF [3] does not have the ability to represent the retro-reflective behavior in the observations. The main reason is because the sum-of-lobes model in [3] was originally proposed under the assumption that both lighting and viewing directions are static, so the dependency on  $l^T v$  was not considered in the model. Therefore, our derived bivariate inverse model also has trouble with handling retro-reflections which violates the monotonicity assumption for  $l^T v$  (i.e., (L5) in our submission). To clarify this point, we categorized reflections into three classes i.e., diffuse, specular (including off-specular reflection) and retro reflection as illustrated in Fig. 1-(a). As illustrated, a retro-reflection provides smaller luminance as the difference between incident and ongoing directions increases (i.e.,  $I \propto l^T v$ ) in an opposite manner of other reflectance lobes. We confirm these phenomena by using some representative materials in MERL BRDF database [8]. In Fig. 1-(b),(d),(f), we illustrated images which were rendered with BRDF of *ipswich-pine-221*, *orange-paint* and *blue-fabric* as examples of specular, diffuse and retro-reflective materials, respectively. In addition to them, plots of  $(l^T v, n^T l, I)$  for fixed surface normal  $n$  and varying lightings  $l$  are illustrated in Fig. 1-(c),(e),(g) by projecting them onto  $l^T v - n^T l$  plane and expressing  $I$  using color (red plot has a large intensity). We observe that only *blue-fabric* violates our assumption i.e.,  $I$  is non-increasing for  $l^T v$ , which coincides with the observation that our naive method without retro-detection scheme had difficulty in *blue-fabric* as shown in Sec. 4.2 of our submission.

### 2.2. Why our method uses a linear regression for detecting retro-reflections?

As mentioned in Sec. 3 of our submission, our method handles retro-reflective reflections by adaptively switching the constraint for  $l^T v$  on the regression problem (i.e.,  $\partial f/\partial y \leq 0$  or  $\partial f/\partial y \geq 0$  in (L5) of our submission). While effective

as shown in Sec. 4.2 of our submission, we should note that this strategy is theoretically problematic in the case where *both* specularities and retro-reflections are simultaneously observed *i.e.*, there is no monotonic variation of  $I$  in the  $\mathbf{l}^T \mathbf{v}$  direction. However, we also note that these case are merely observed in the natural world, and if any, our retro-reflection detection algorithm still improves the result since there is usually one *dominant reflection* which provides more appropriate constraint for the problem. Furthermore, our regression scheme based on robust Bernstein polynomials usually suppresses the estimation errors caused by the non-dominant reflections (those observations are supported by our experimental results using MERL BRDF database [8] which are illustrated in Fig. 6 of our submission and Fig. 5-104 of this supplementary).

Assuming that the reflectance function as for fixed surface normal has one preferable monotonicity for  $\mathbf{l}^T \mathbf{v}$  which would give more accurate estimation of the surface normal, the problem is, as described in our submission, how can we find the direction of monotonicity. As mentioned in Sec. 3 of our submission, we overcame this difficulty by three steps: (a) estimating surface normals under both constraints, (b) computing regression errors with recovered surface normals, (c) adopting the surface normal with smaller errors as the final estimation. As described in our submission, we have examined two kind of regression errors from Eq. (15) and Eq. (17) of our submission. In Fig. 2, we illustrate the regression results based on two constraints (*i.e.*,  $\partial g / \partial y \geq 0$  or  $\partial g / \partial y \leq 0$  in (L9) of our submission), where plots of  $(\mathbf{l}^T \mathbf{v}, I, \mathbf{n}^T \mathbf{l})$  were overlaid with reconstructed inverse reflectance function represented by Bernstein polynomials (each case is presented from two viewpoints). In addition, we also show regression errors from Eq. (15) and Eq. (17) for each material and an angular error of surface normal at the bottom of plots. As observed, regression errors from Eq. (15) do not work for determining appropriate constraint in *blue-fabric* since the flexible Bernstein polynomials were well fitted to observations even though the constraint was not correct. On the other hand, the linear regression error from Eq. (15) reasonably increased in both *blue-fabric* and *ipswich-pine-221* when the constraint was incorrect. We observed this relationship for most materials in MERL BRDF database, that is why we adopted the linear regression error for our retro-reflection detection algorithm.

### 3. Appendix C: Details about BRDF Models Used in Sec. 4.1

This appendix expands on the detailed description about the isotropic BRDF which were used for rendering synthetic images in Sec. 4.1 of our submission. For further information of each BRDF, we recommend readers to refer a recent survey by Montes and Urena [9]. We show input images rendered with those BRDF which were used in Sec. 4.1 of our submission in Fig. 3.

#### 3.1. Cook-Torrance Model [4]

Cook-Torrance model represents the reflection using a combination of diffuse and specular parts as

$$\rho(\mathbf{n}, \mathbf{l}, \mathbf{v}) = \frac{k_d}{\pi} + k_s f_S(\mathbf{n}, \mathbf{l}, \mathbf{v}, \lambda_1, \mu_1). \quad (2)$$

Here  $k_d$  and  $k_s$  are model parameters representing the strength of diffuse and specular terms respectively.  $f_S$  is a nonlinear function which is represented as

$$f_S(\mathbf{n}, \mathbf{l}, \mathbf{v}, \lambda_1, \mu_1) = \frac{F(\mathbf{l}, \mathbf{v}, \lambda_1)}{\pi} \frac{D(\mathbf{n}, \mathbf{l}, \mathbf{v}, \mu_1)G(\mathbf{n}, \mathbf{l}, \mathbf{v})}{(\mathbf{n}^T \mathbf{v})(\mathbf{n}^T \mathbf{l})}, \quad (3)$$

where  $F$  is the Fresnel factor,  $D$  is the microfacets distribution which is computed by the Beckmann distribution function and  $G$  is the geometric attenuation factor, respectively. We use the same  $D$  and  $G$  in [4] and use the Schlick approximation of the Fresnel term ( $F$ ) [11] as follow:

$$F(\mathbf{l}, \mathbf{v}, \lambda_1) = \lambda_1 + (1 - \lambda_1)(1 - \mathbf{l}^T \mathbf{h})^5, \quad (4)$$

where  $\lambda$  is the reflection coefficient for light incoming parallel to the normal, and  $\mathbf{h}$  is a half vector as  $\mathbf{h} = (\mathbf{l} + \mathbf{v}) / |\mathbf{l} + \mathbf{v}|$ .

In the Cook-Torrance model, the diffuse reflection is represented by a linear Lambertian reflection [14] and the specular reflection is modeled by a specular lobe which is pointing at the normalized half vector (smaller roughness parameter  $\mu_1$  provides narrower specular highlight) and Fresnel effect, increasing the specular reflectivity as the surface turns away from the viewing direction. In our submission, we used  $k_d = 0.9$ ,  $k_s = 0.1$ ,  $\lambda = 0.2$  and  $\mu_1 = 0.2$ , respectively.

### 3.2. Ward Model [13]

Ward model also represents the reflection in the same form of Eq. (2) in Cook-Torrance model, however this model only extracts the microfacets distribution  $D$  in Eq. (3) for representing the specular reflection as follow

$$f_S(\mathbf{n}, \mathbf{l}, \mathbf{v}, \mu_2) = \frac{1}{4\pi\mu_2^2\sqrt{(\mathbf{n}^T\mathbf{l})(\mathbf{n}^T\mathbf{v})}} \exp\left(\frac{1}{\mu_2^2}\left(1 - \frac{1}{\mathbf{n}^T\mathbf{h}^2}\right)\right), \quad (5)$$

where  $\mu_2$  is the roughness parameter which determines the size of specular highlight (smaller roughness parameter  $\mu_2$  provides narrower specular highlight). In the Ward model, the diffuse reflection is also represented by a linear Lambertian reflection [14]. In our submission, we used  $\mu_2 = 0.2$ . We note that specular highlights rendered with Cook-Torrance and Ward BRDF are mainly distributed in the high-frequency observations (*i.e.*, observations with large intensities), therefore, effects of those specularities are easily neglected by discarding input observations whose intensities are relatively large (*i.e.*,  $T_{low} < 50\%$  in our submission).

### 3.3. Lafortune Model [6]

Lafortune model is one of the most multifunctional BRDF models which is able to represent the data from real materials which have more than one lobe. In our experiment, we use this model to represent the general diffuse reflection which is more complex than a simple Lambertian reflection used in the Cook-Torrance and Ward BRDF.

As shown by Lin and Lee [7], a general rotationally symmetric diffuse component in the Lafortune model is represented as

$$\rho(\mathbf{n}, \mathbf{l}, \mathbf{v}) = (\mathbf{n}^T\mathbf{l})^k (\mathbf{n}^T\mathbf{v})^k, \quad (6)$$

where  $k$  is a model parameter which determines the non-linearity of the function. In our submission, we rendered images with only diffuse component without off-specular component in the Lafortune model to verify performance of each algorithm to handle complex non-linear diffuse reflections. In our submission, we used  $k = 0.5$ .

### 3.4. Oren-Nayar Model [10]

Oren-Nayar model is derived from Lambertian model [14] to explain the view dependency of the matte or rough surfaces with geometric optics. While this model and Oren-Nayar model both represent non-Lambertian diffuse reflections, this model can represent retro-reflective behavior of non-Lambertian diffusive objects unlike Lafortune BRDF.

The Oren-Nayar model is represented as follow

$$\rho(\mathbf{n}, \mathbf{l}, \mathbf{v}) = \frac{1}{\pi} (A + B \max(0, \cos(\phi_i - \phi_o)) \sin \alpha \tan \beta), \quad (7)$$

where  $\phi_i$  and  $\phi_o$  are differential angles as for  $\mathbf{l}$  and  $\mathbf{v}$  respectively, and  $a, b, A$  and  $B$  are written as

$$a = \max(\cos^{-1}(\mathbf{n}^T\mathbf{l}), \cos^{-1}(\mathbf{n}^T\mathbf{v})) \quad b = \min(\cos^{-1}(\mathbf{n}^T\mathbf{l}), \cos^{-1}(\mathbf{n}^T\mathbf{v})). \quad (8)$$

and

$$A = 1 - 0.5 \frac{\alpha^2}{\alpha^2 + 0.33} \quad B = 0.45 \frac{\alpha^2}{\alpha^2 + 0.09}. \quad (9)$$

Here,  $\alpha$  determines the surface roughness and it is equivalent to the Lambertian model in the case of  $\alpha = 0$ . In our submission, we fixed the roughness parameter  $\alpha$  by 0.5.

### 3.5. Ashikhmin-Shirley Model [2]

Ashikhmin-Shirley model is expressed as a weighted sum of the diffuse and specular term as

$$\rho(\mathbf{n}, \mathbf{l}, \mathbf{v}) = \frac{k_d}{\pi} f_D(\mathbf{n}, \mathbf{l}, \mathbf{v}) + k_s f_S(\mathbf{n}, \mathbf{l}, \mathbf{v}, \lambda_2, \mu_3). \quad (10)$$

The non-linear diffuse term  $f_D$  guarantees the reciprocity and energy conservation properties and is written as

$$f_D(\mathbf{n}, \mathbf{l}, \mathbf{v}) = \frac{28}{23} \left(1 - \left(1 - \frac{\cos(\mathbf{n}^T\mathbf{l})}{2}\right)^5\right) \left(1 - \left(1 - \frac{\cos(\mathbf{n}^T\mathbf{v})}{2}\right)^5\right). \quad (11)$$

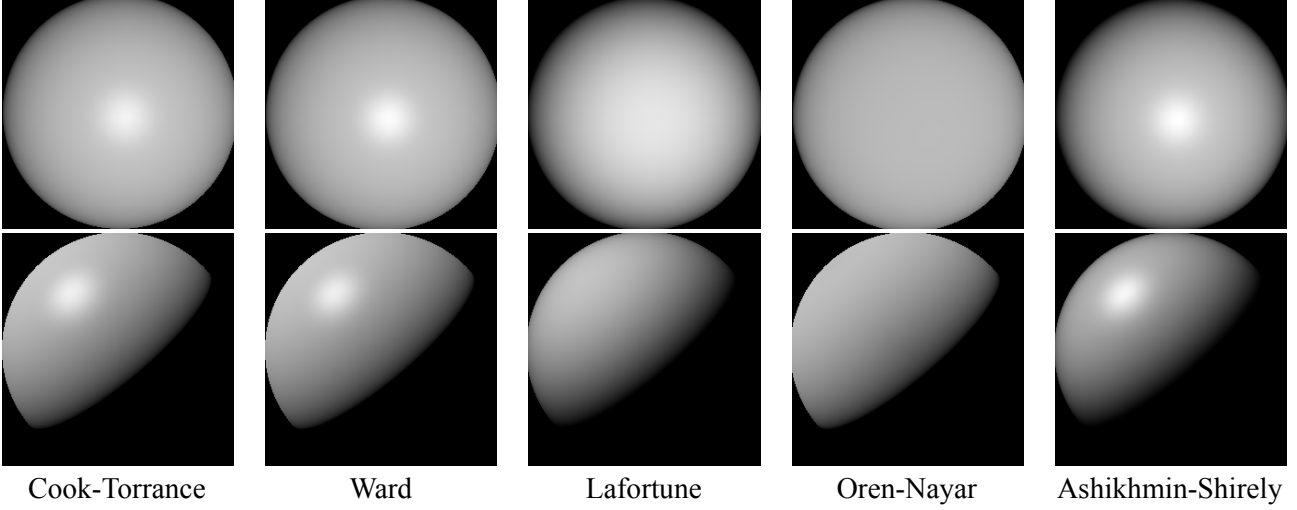


Figure 3. Input images rendered with five different BRDF which were used in Sec. 4.1 of our submission.

The specular term uses the distribution over the half vector in the similar manner with Cook-Torrance model [4] as

$$f_S(\mathbf{n}, \mathbf{l}, \mathbf{v}, \lambda_2, \mu_3) = \frac{F(\mathbf{l}, \mathbf{v}, \lambda_2)}{\pi} \frac{D(\mathbf{n}, \mathbf{l}, \mathbf{v}, \mu_3)}{8\pi(\mathbf{h}^T \mathbf{l}) \max(\mathbf{n}^T \mathbf{l}, \mathbf{n}^T \mathbf{v})}, \quad (12)$$

where  $F$  is the Schlick's approximation of Fresnel term and  $D$  is a microfacet distribution function described as

$$F(\mathbf{l}, \mathbf{v}, \lambda_2) = (\mu_3 + 1)(\mathbf{n}^T \mathbf{h})^{\mu_3}, \quad (13)$$

where  $\mu_3$  controls the roughness of the material which was fixed by 50 in our submission.

#### 4. Appendix D: Details of Results Using MERL BRDF database in Sec. 4.2

This appendix provides a full experimental results using MERL BRDF database [8] which were shown in Fig. 6 in Sec. 4.2 of our submission. In Fig. 5 to Fig. 104, we illustrate input images, recovered surface normal maps and corresponding error maps for 100 materials in alphabetical order. We also show 3-d plots of  $(\mathbf{l}^T \mathbf{v}, \mathbf{n}^T \mathbf{l}, I)$  for three different surface normals which were projected onto the  $\mathbf{l}^T \mathbf{v} - \mathbf{n}^T \mathbf{l}$  space, whose plots were colored by its intensity. We have provided those information so that readers can examine how our method or other methods performed on each material in Fig. 6 of our submission.

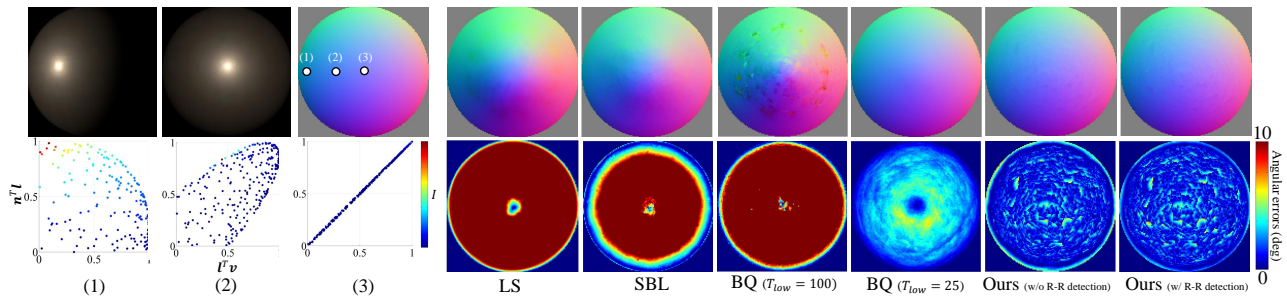


Figure 4. The results of alum-bronze.

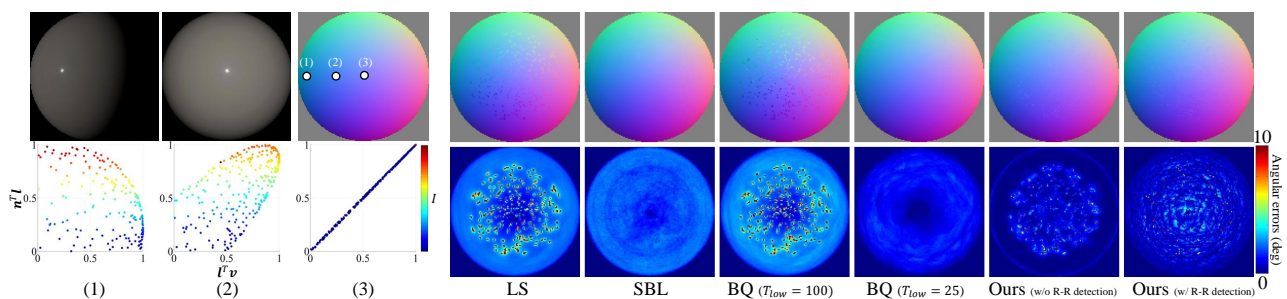


Figure 5. The results of alumina-oxide.

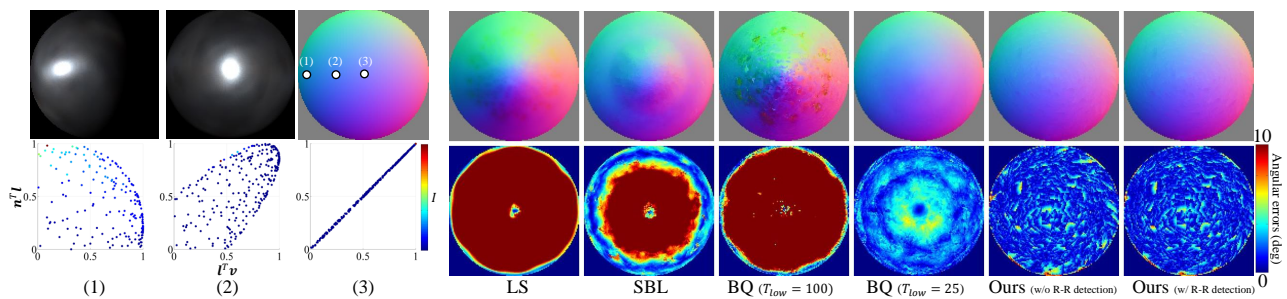


Figure 6. The results of aluminium.

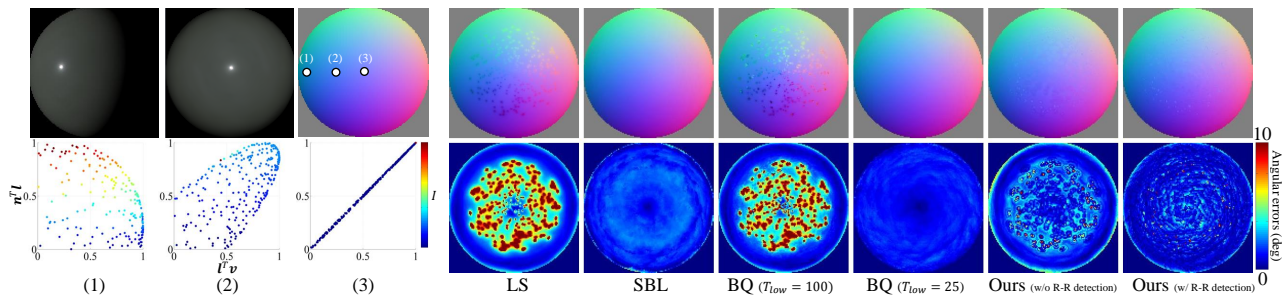


Figure 7. The results of aventurine.

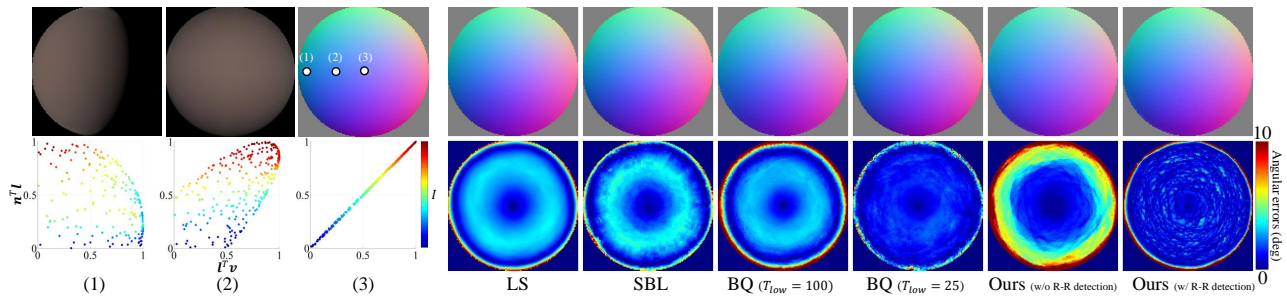


Figure 8. The results of beige-fabric.

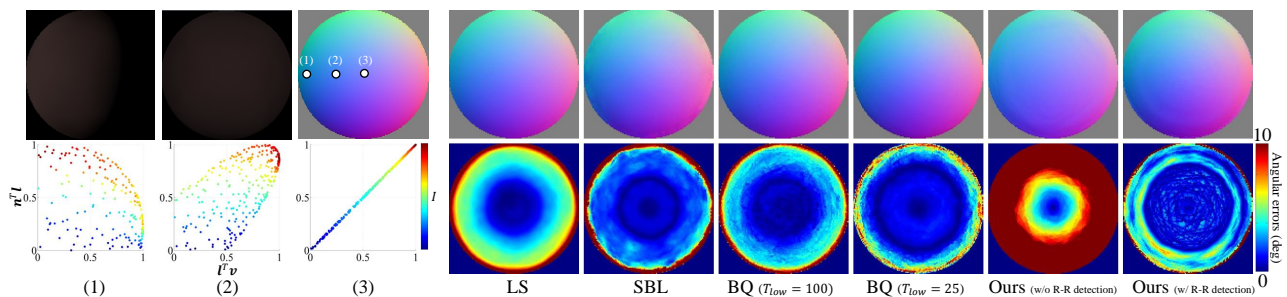


Figure 9. The results of black-fabric.

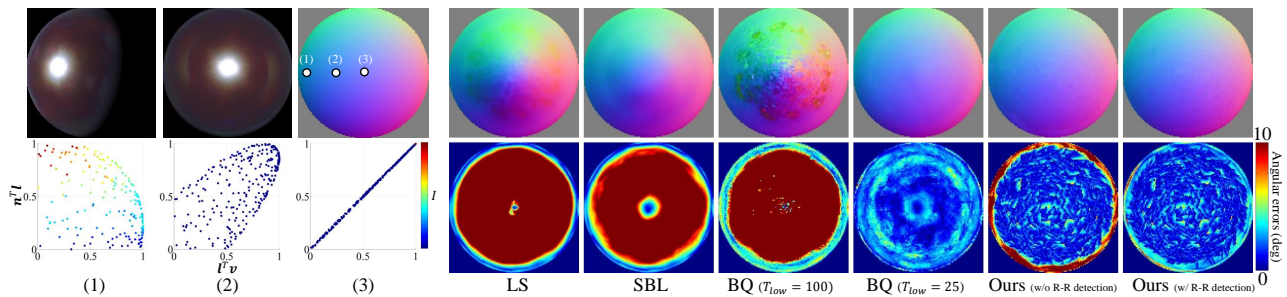


Figure 10. The results of black-obsidian.

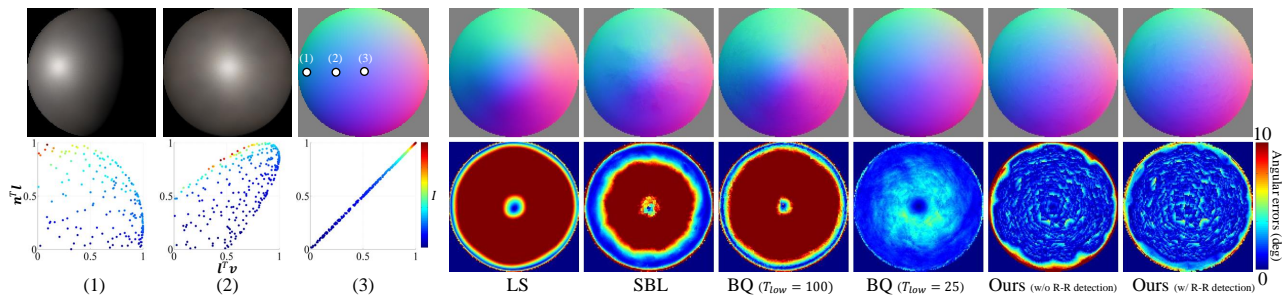


Figure 11. The results of black-oxidized-steel.

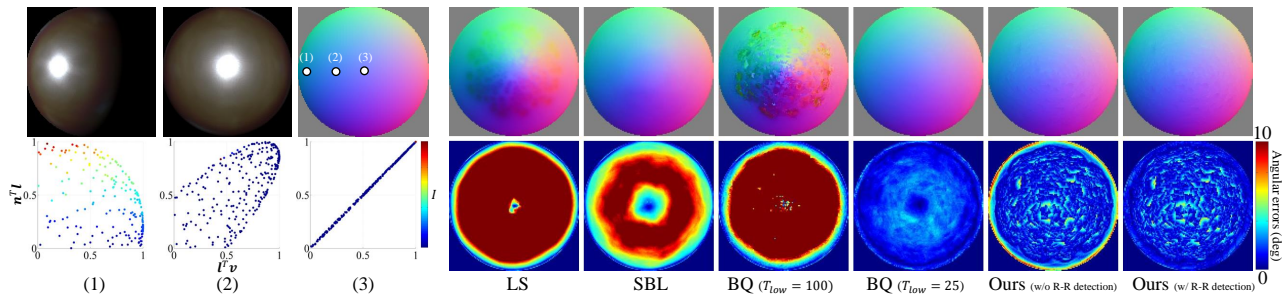


Figure 12. The results of black-phenolic.

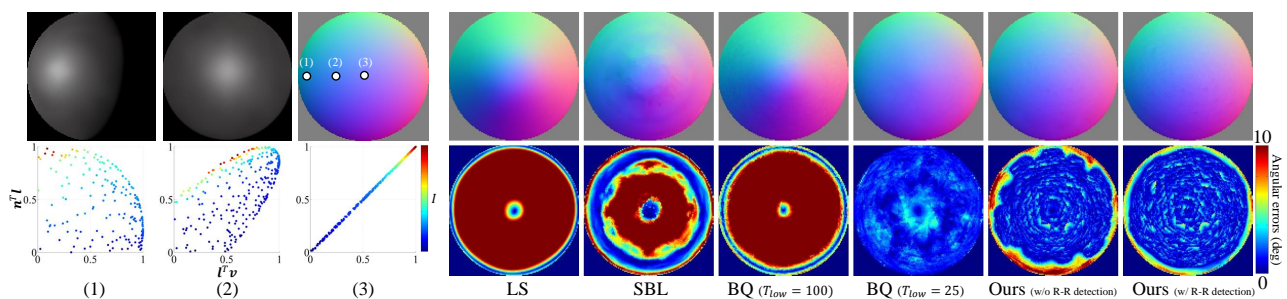


Figure 13. The results of black-soft-plastic.

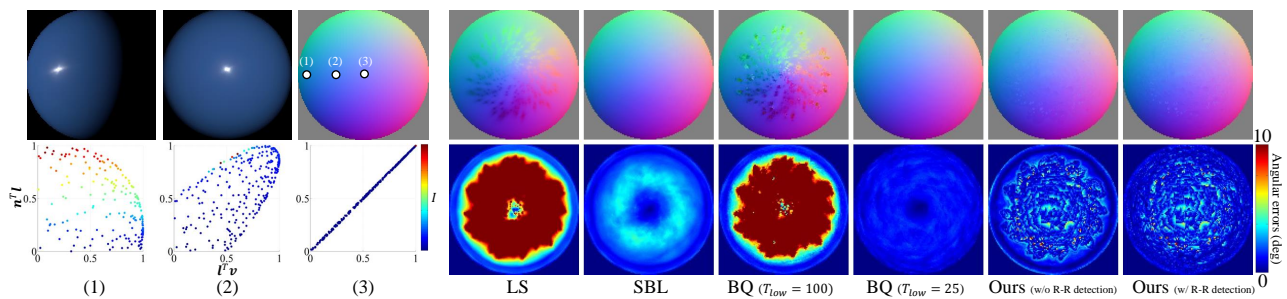


Figure 14. The results of blue-acrylic.

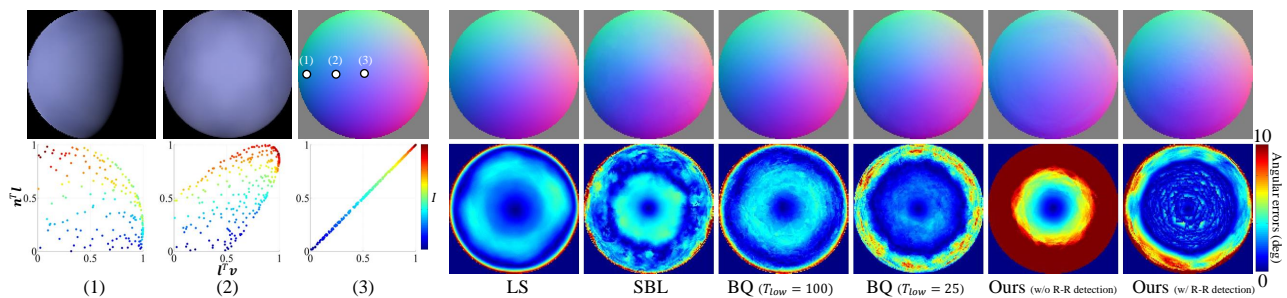


Figure 15. The results of blue-fabric.

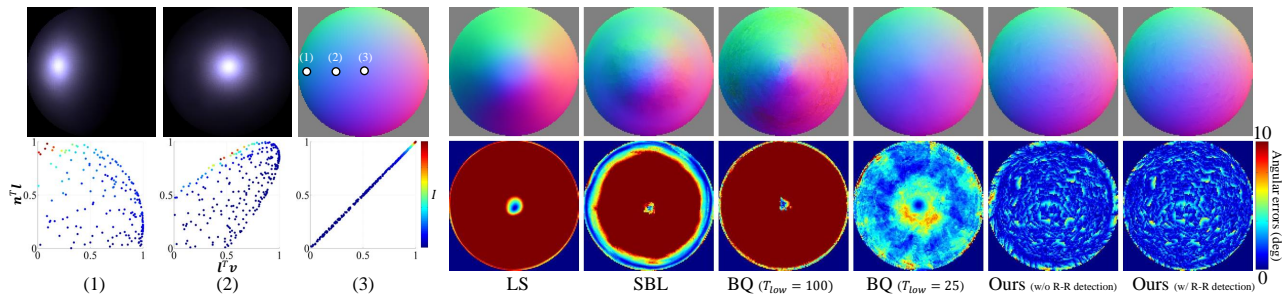


Figure 16. The results of blue-metallic-paint.

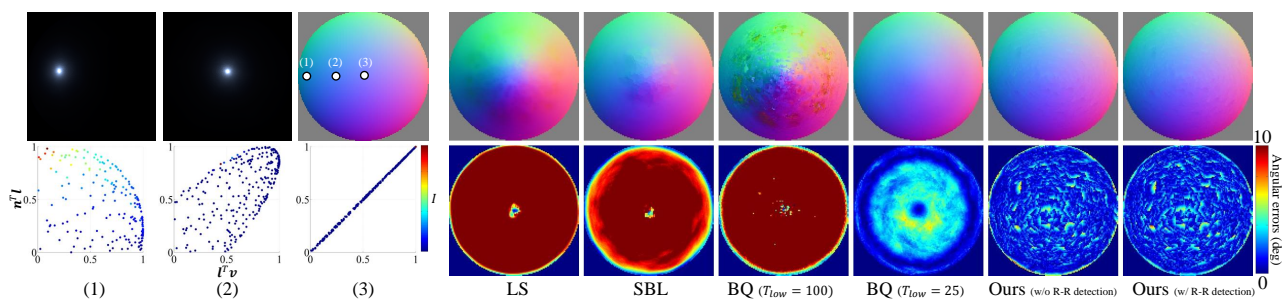


Figure 17. The results of blue-metallic-paint2.

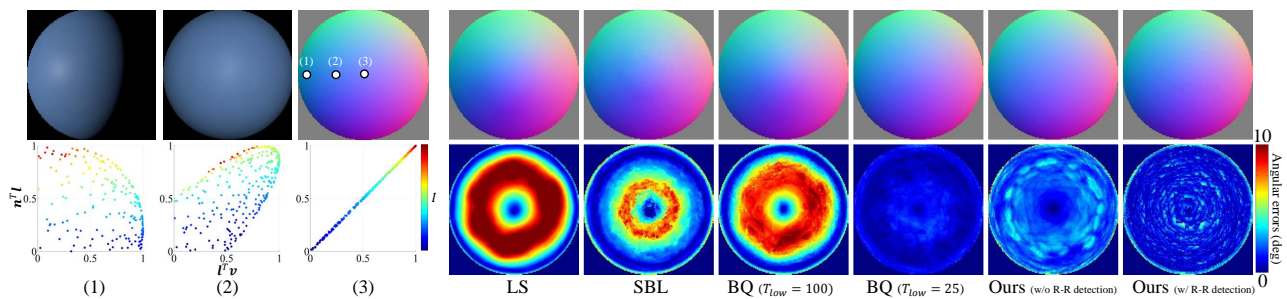


Figure 18. The results of blue-rubber.

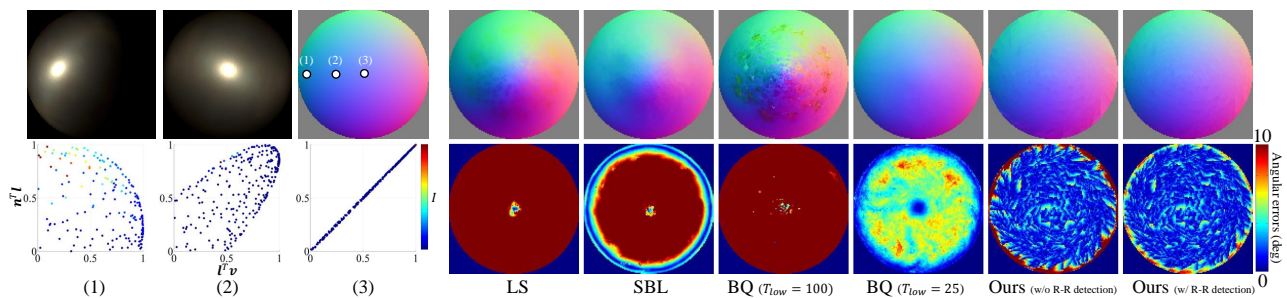


Figure 19. The results of brass.

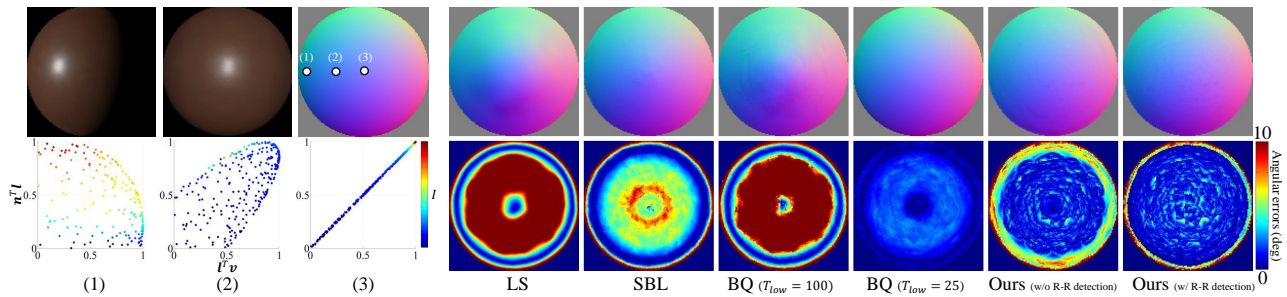


Figure 20. The results of cherry-235.

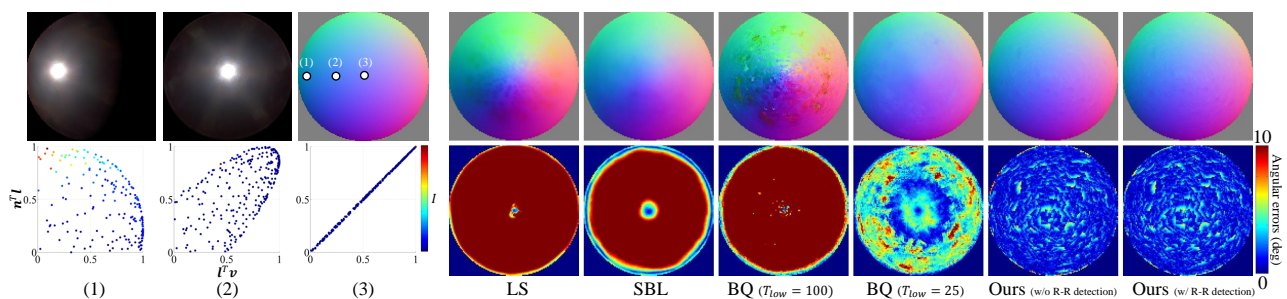


Figure 21. The results of chrome.

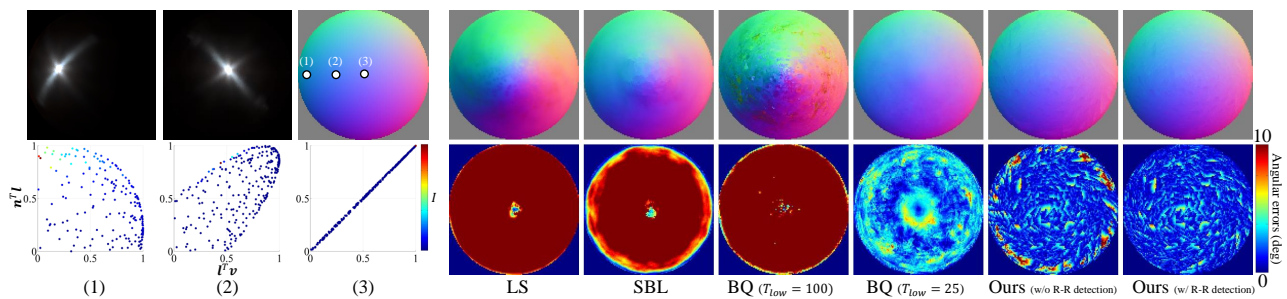


Figure 22. The results of chrome-steel.

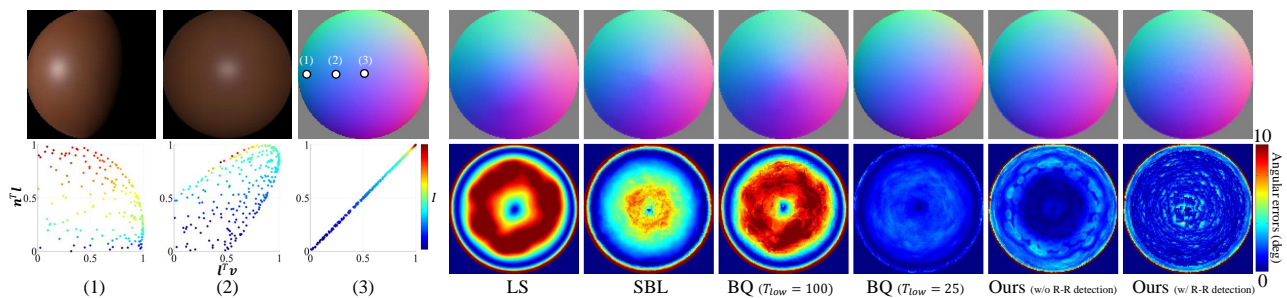


Figure 23. The results of colonial-maple-223.

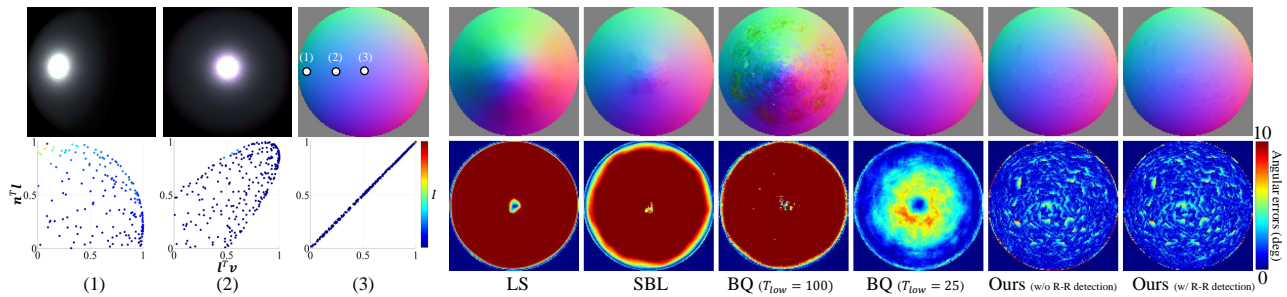


Figure 24. The results of color-changing-paint1.

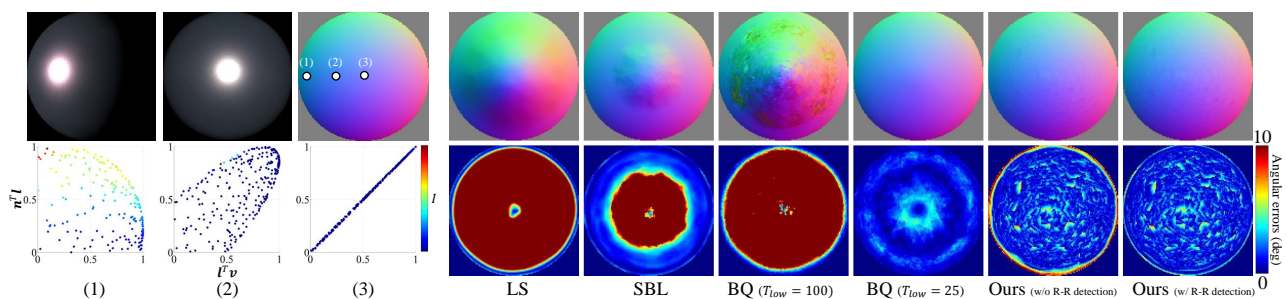


Figure 25. The results of color-changing-paint2.

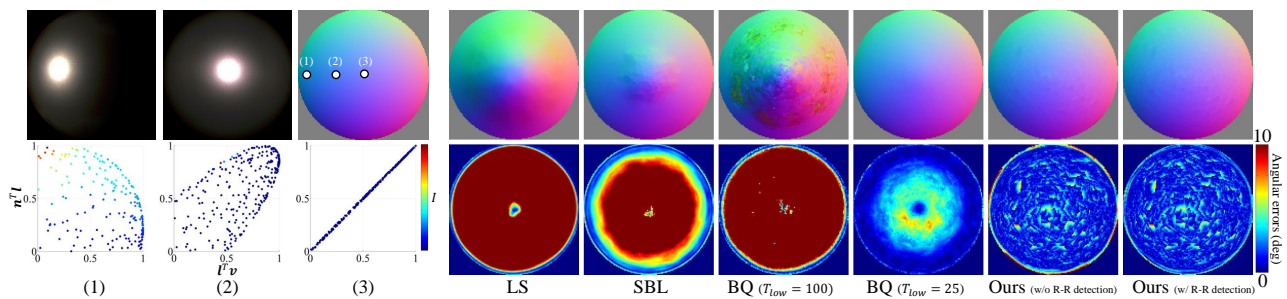


Figure 26. The results of color-changing-paint3.

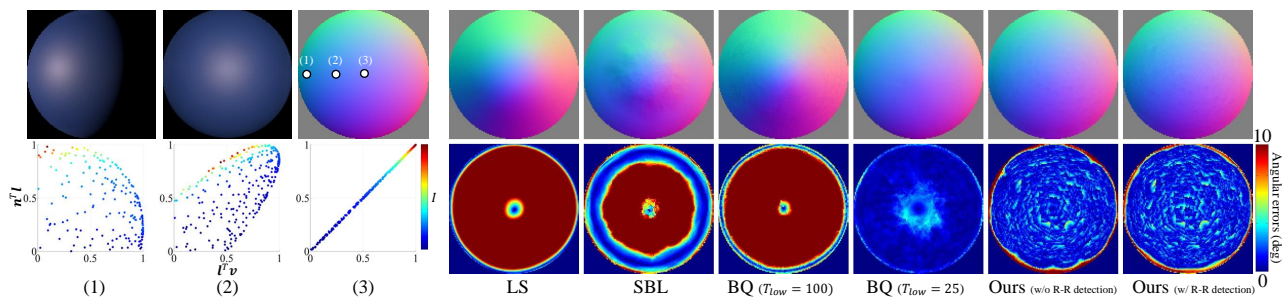


Figure 27. The results of dark-blue-paint.

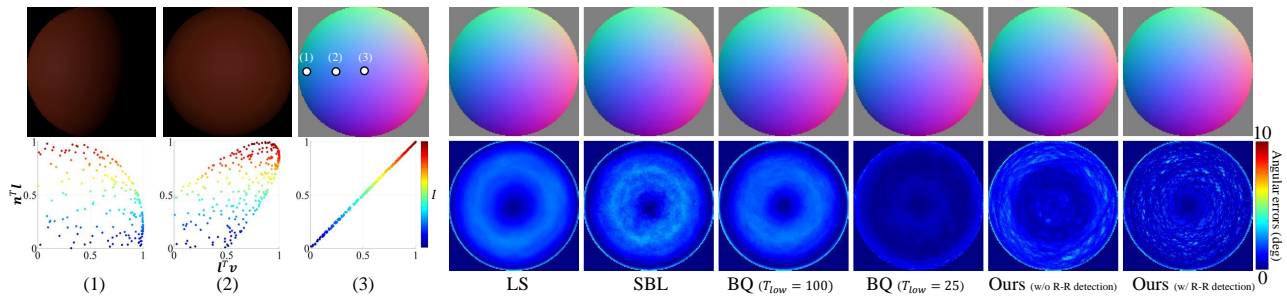


Figure 28. The results of dark-red-paint.

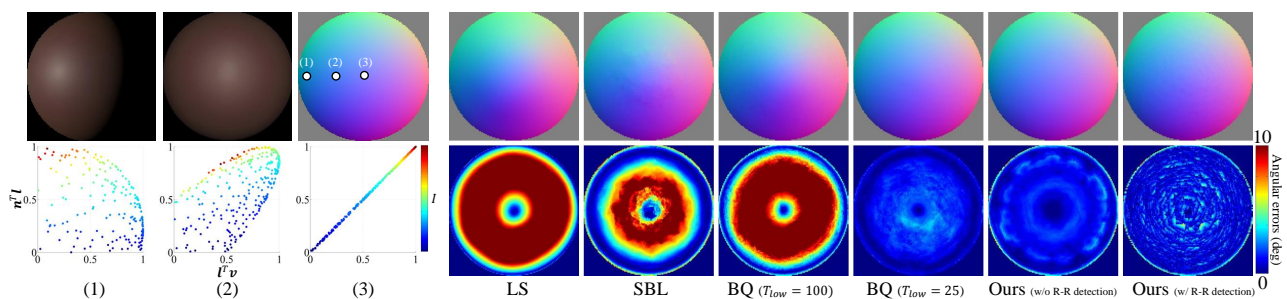


Figure 29. The results of dark-specular-fabric.

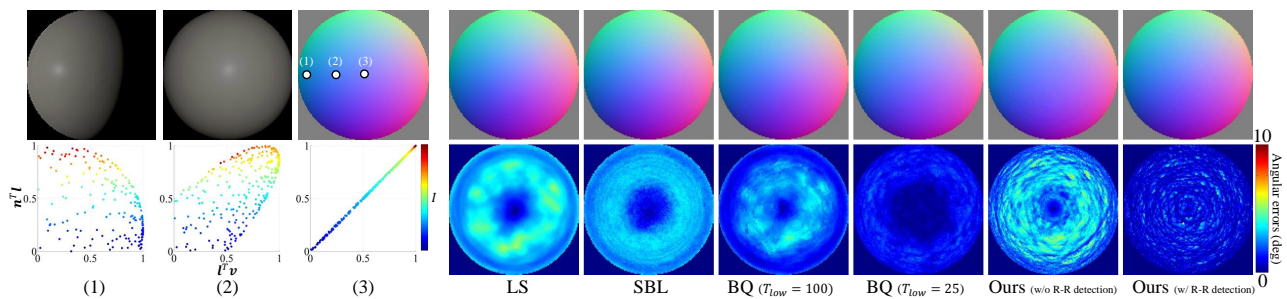


Figure 30. The results of delrin.

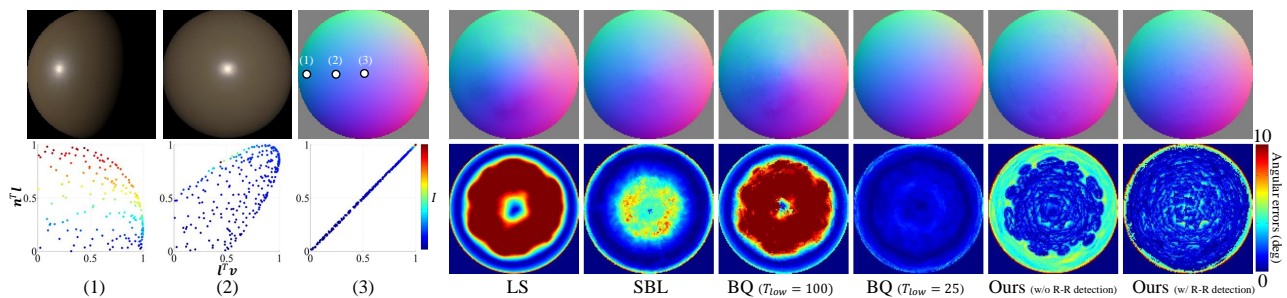


Figure 31. The results of fruitwood-241.

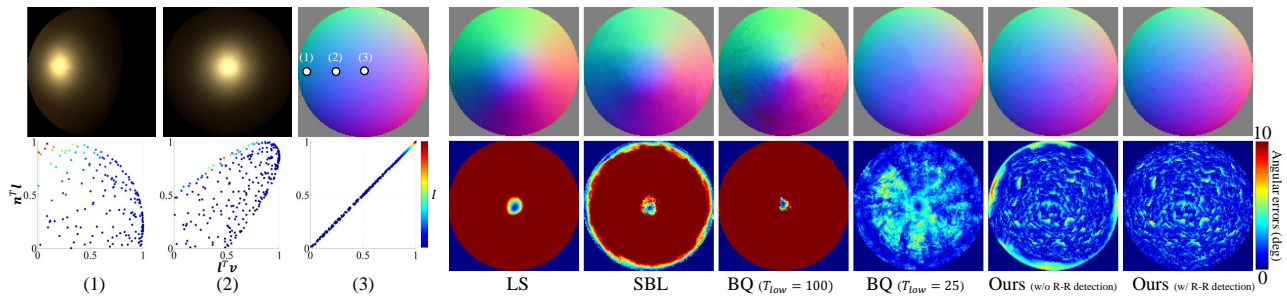


Figure 32. The results of gold-metallic-paint.

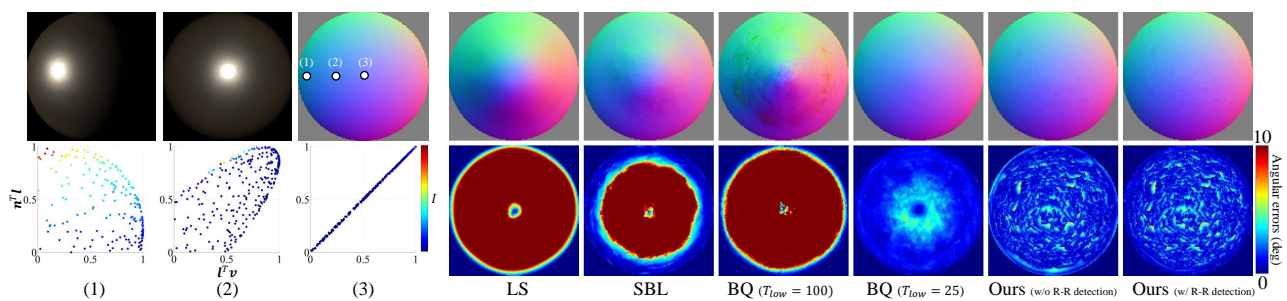


Figure 33. The results of gold-metallic-paint2.

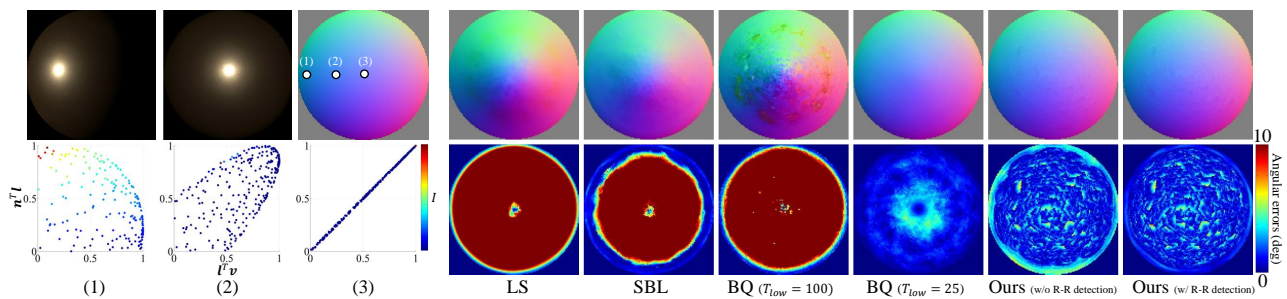


Figure 34. The results of gold-metallic-paint3.

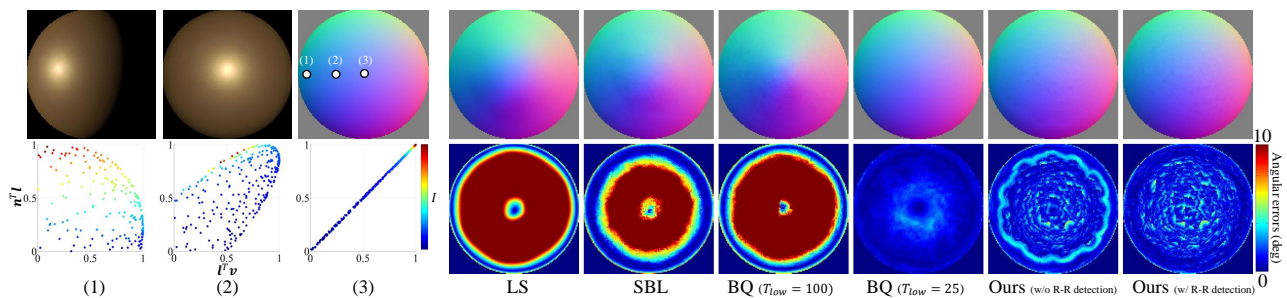


Figure 35. The results of gold-paint.

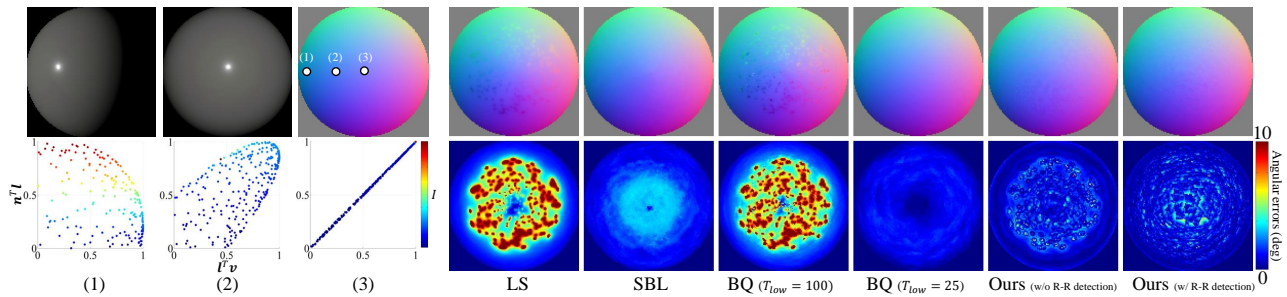


Figure 36. The results of gray-plastic.

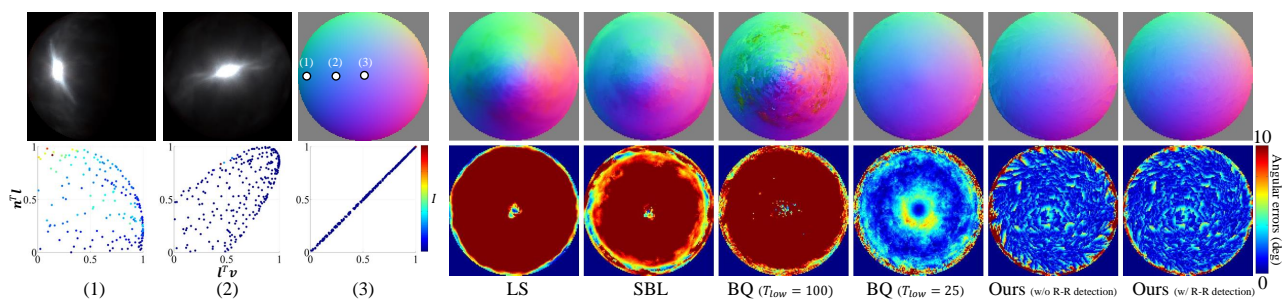


Figure 37. The results of grease-covered-steel.

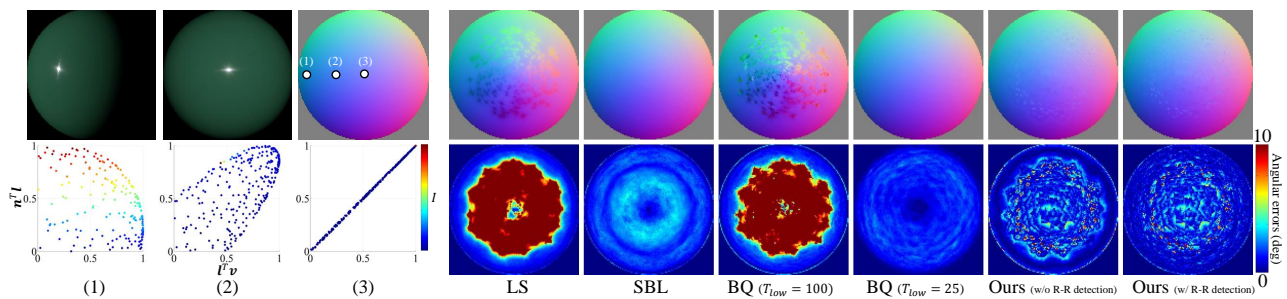


Figure 38. The results of green-acrylic.

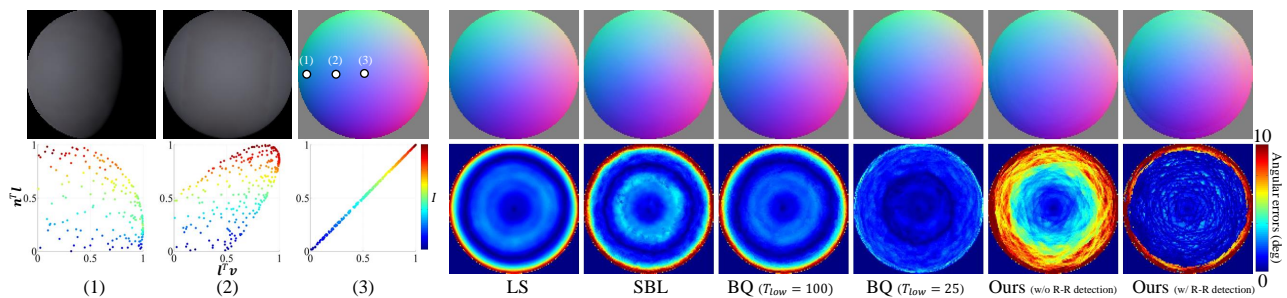


Figure 39. The results of green-fabric.

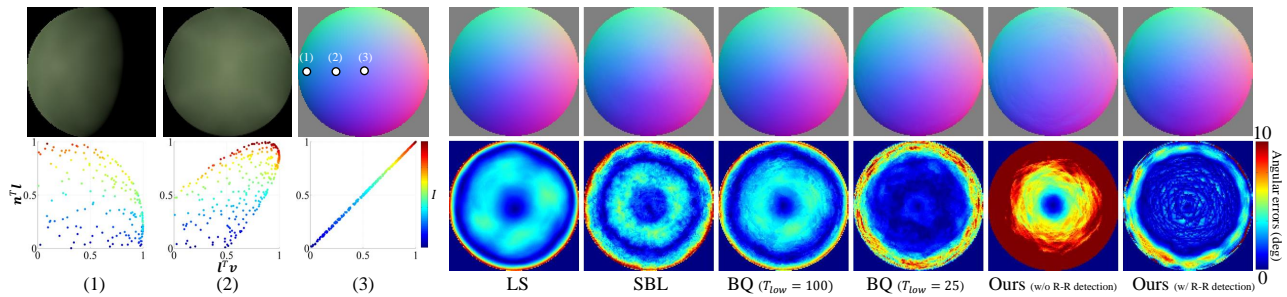


Figure 40. The results of green-latex.

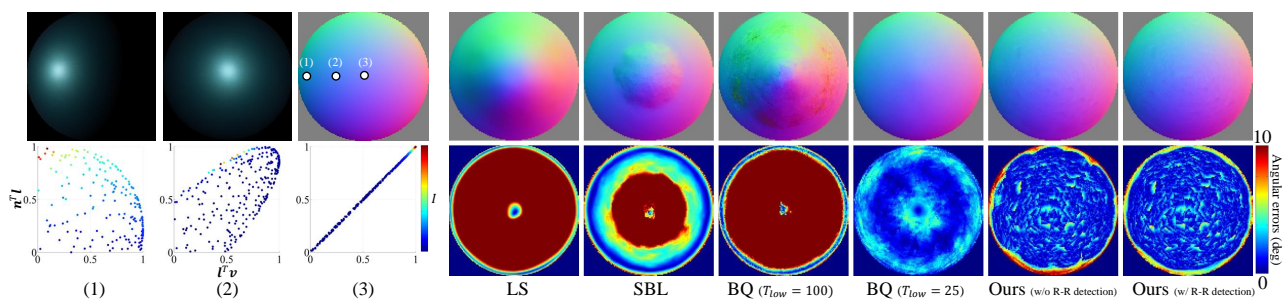


Figure 41. The results of green-metallic-paint.

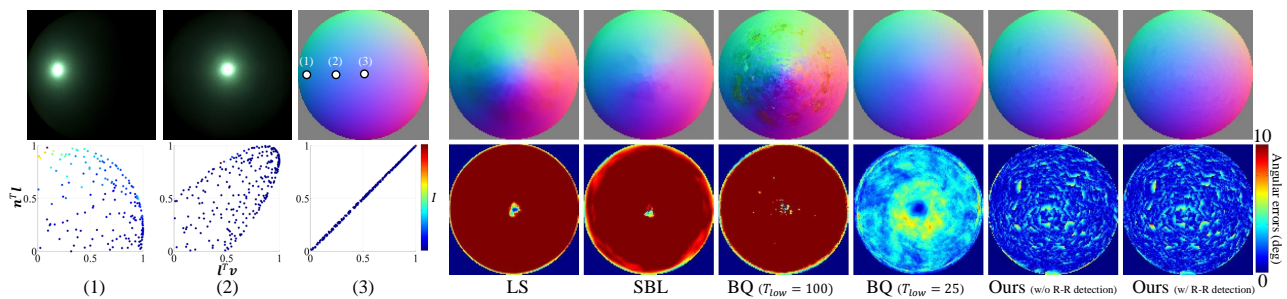


Figure 42. The results of green-metallic-paint2.

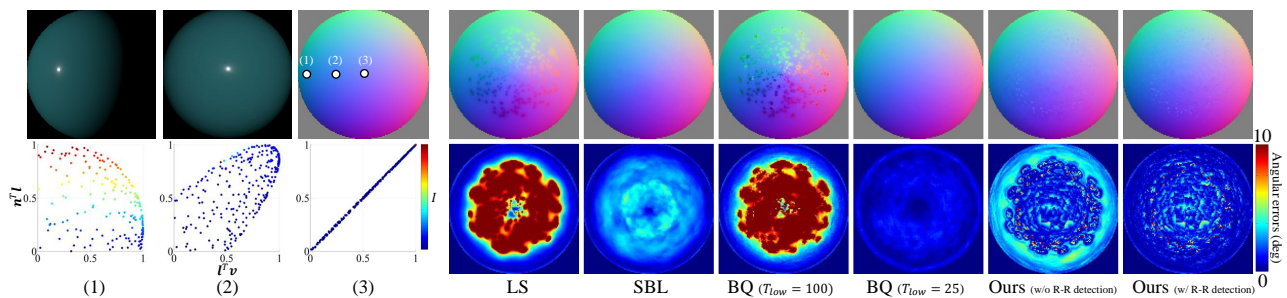


Figure 43. The results of green-plastic.

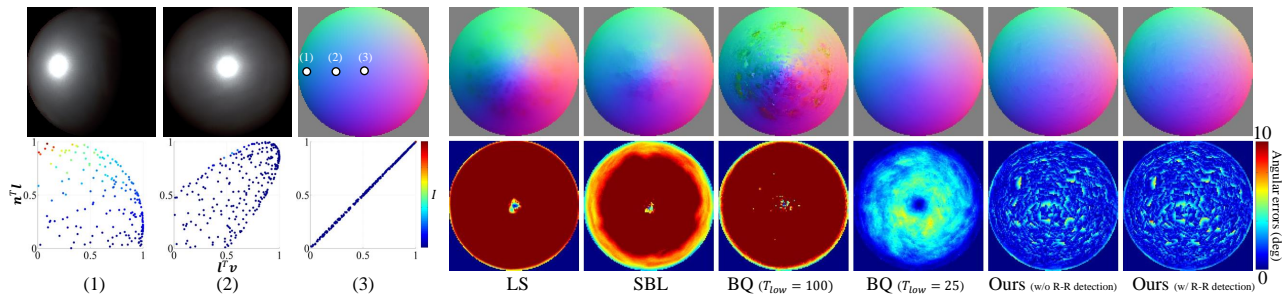


Figure 44. The results of hematite.

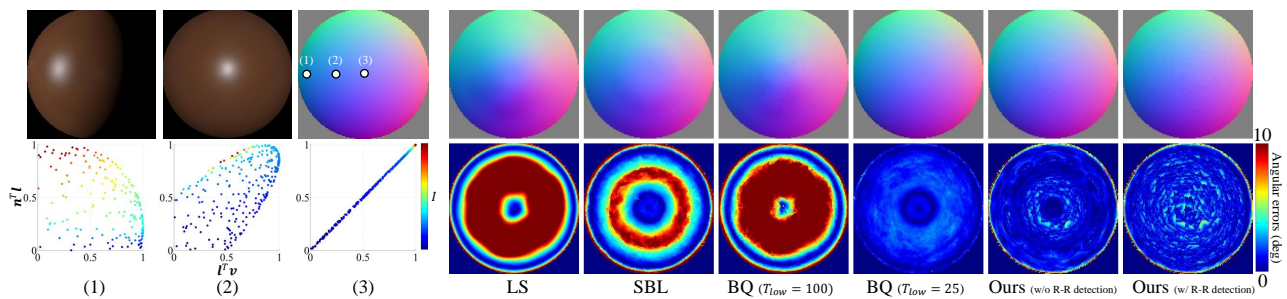


Figure 45. The results of ipswich-pine-221.

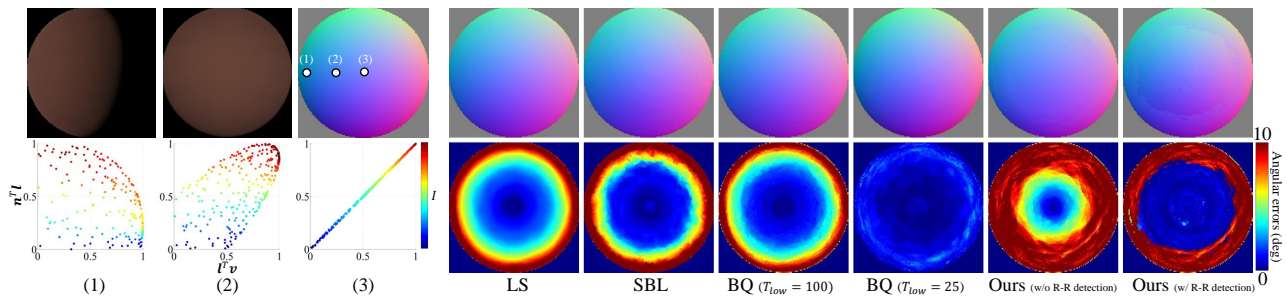


Figure 46. The results of light-brown-fabric.

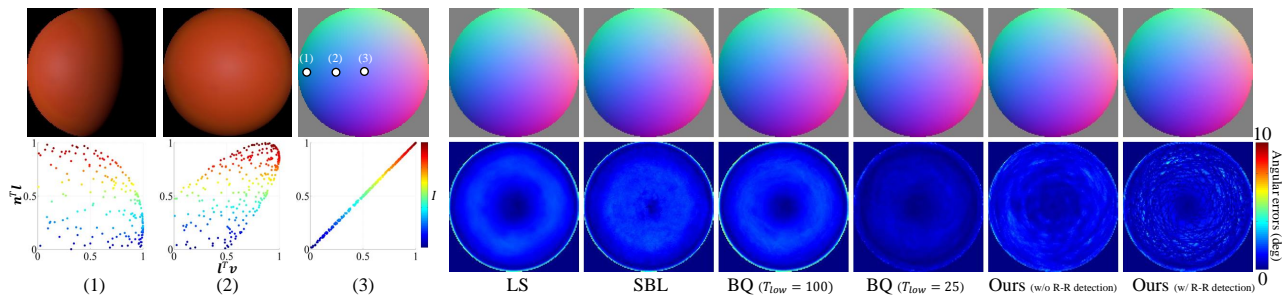


Figure 47. The results of light-red-paint.

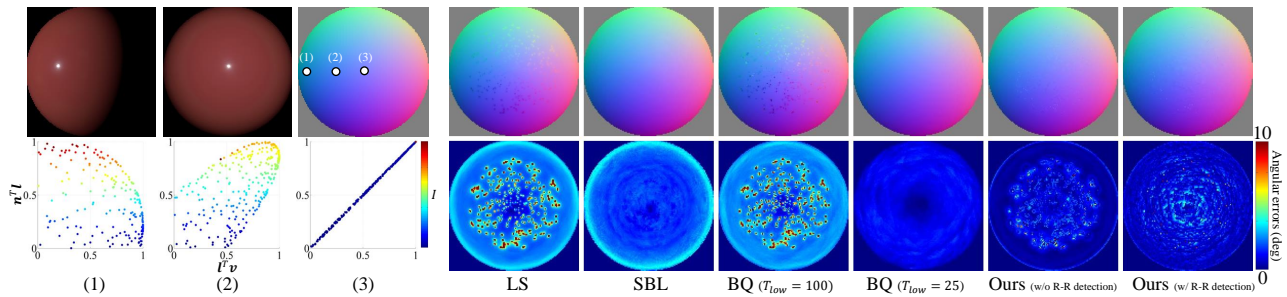


Figure 48. The results of maroon-plastic.

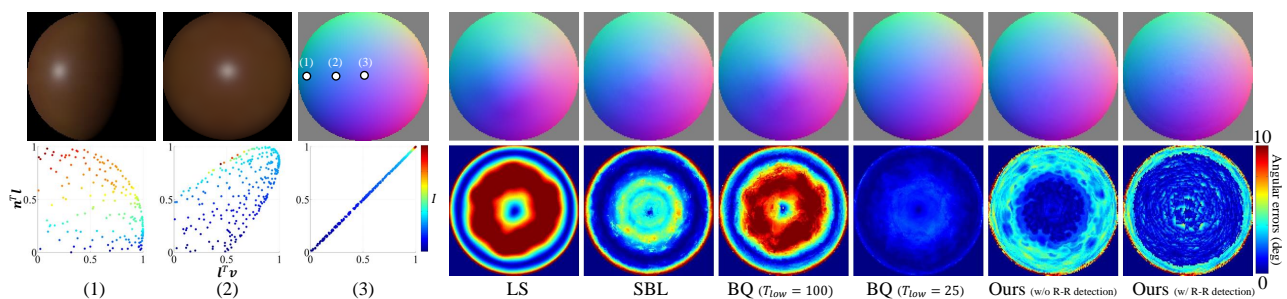


Figure 49. The results of natural-209.

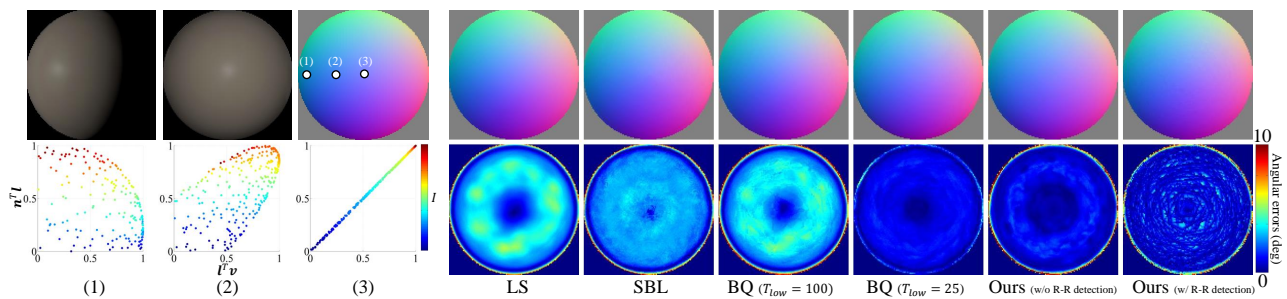


Figure 50. The results of neoprene-rubber.

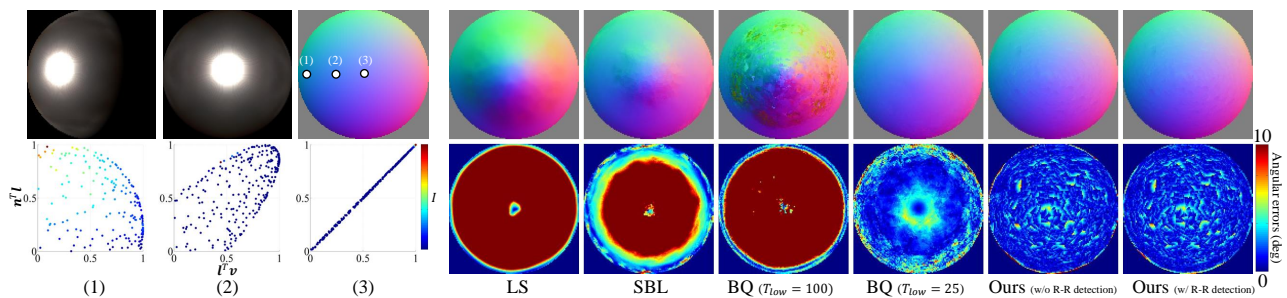


Figure 51. The results of nickel.

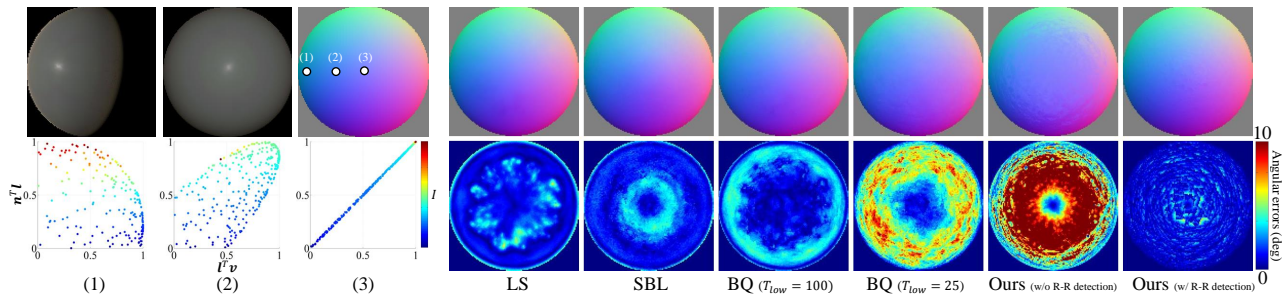


Figure 52. The results of nylon.

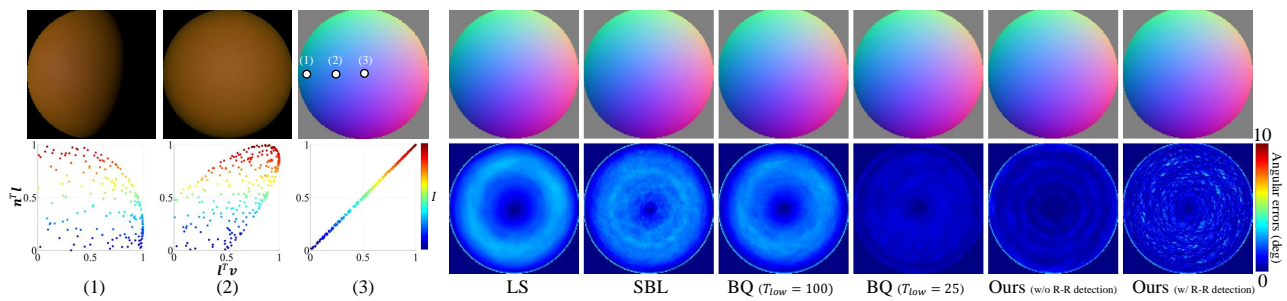


Figure 53. The results of orange-paint.

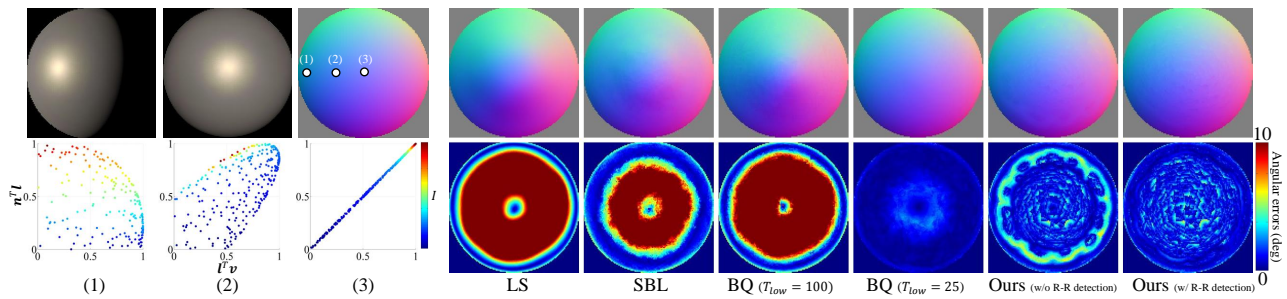


Figure 54. The results of pearl-paint.

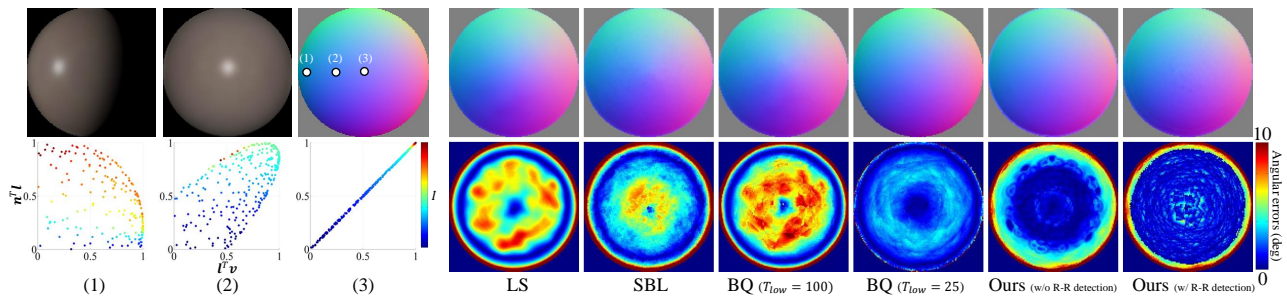


Figure 55. The results of pickled-oak-260.

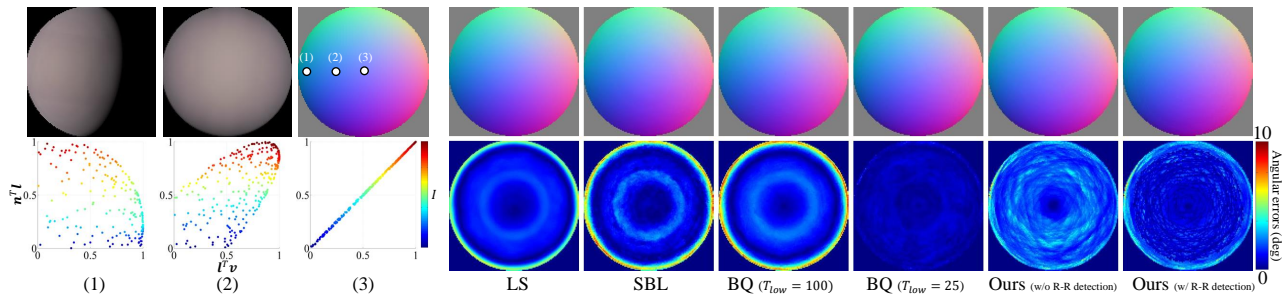


Figure 56. The results of pink-fabric.

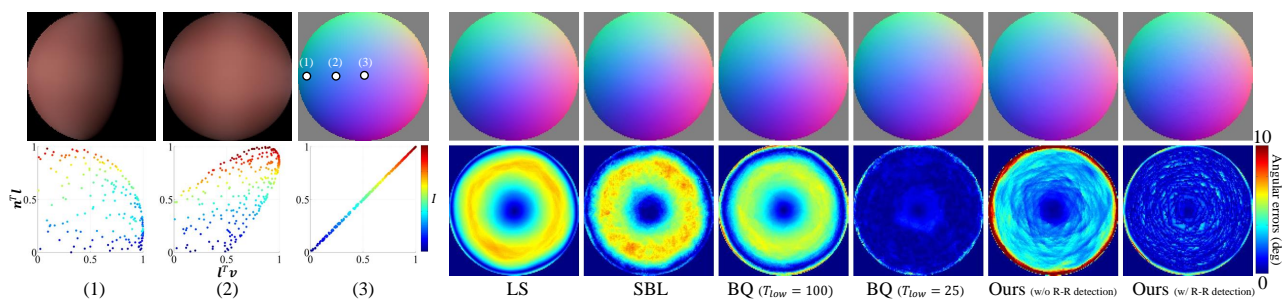


Figure 57. The results of pink-fabric2.

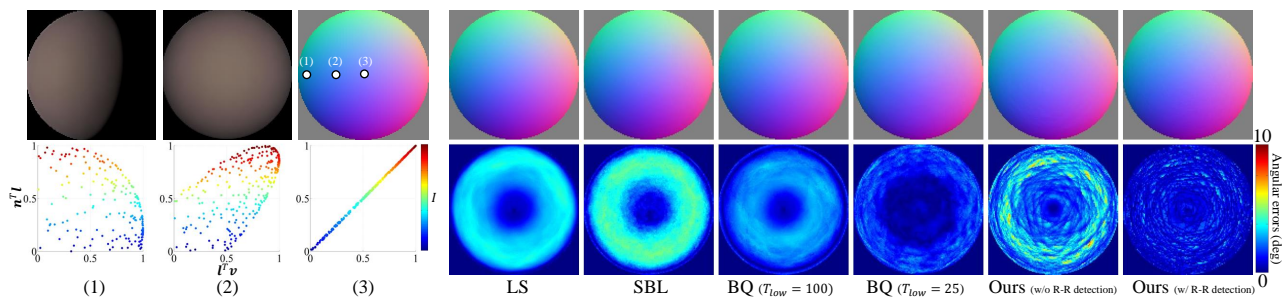


Figure 58. The results of pink-felt.

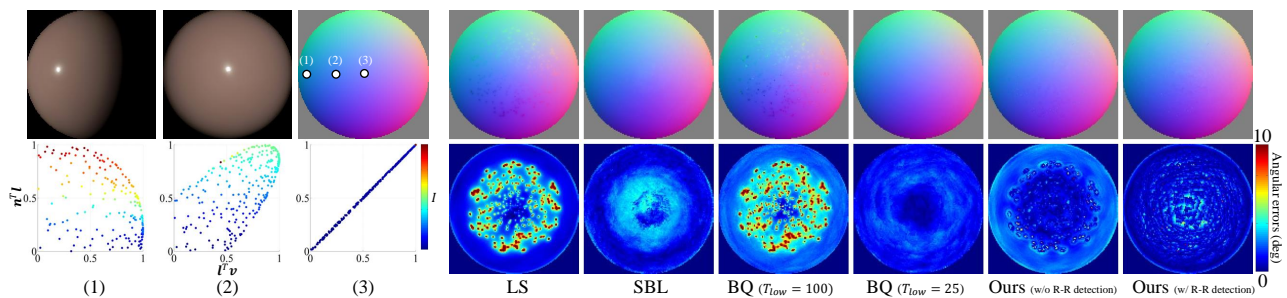


Figure 59. The results of pink-jasper.

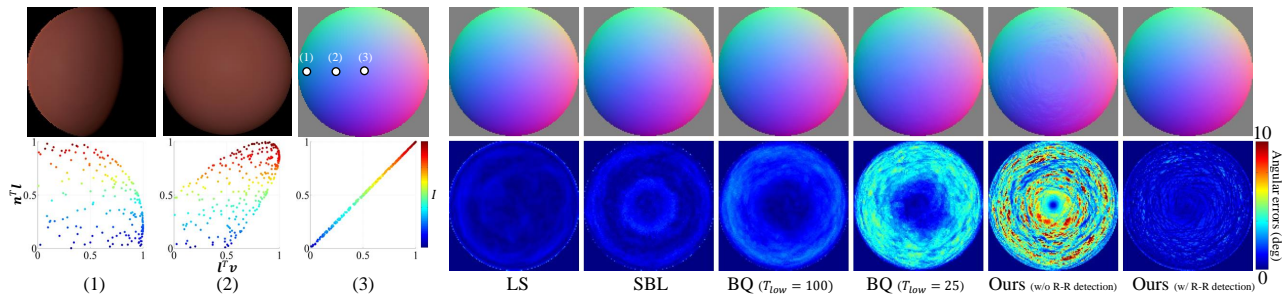


Figure 60. The results of pink-plastic.

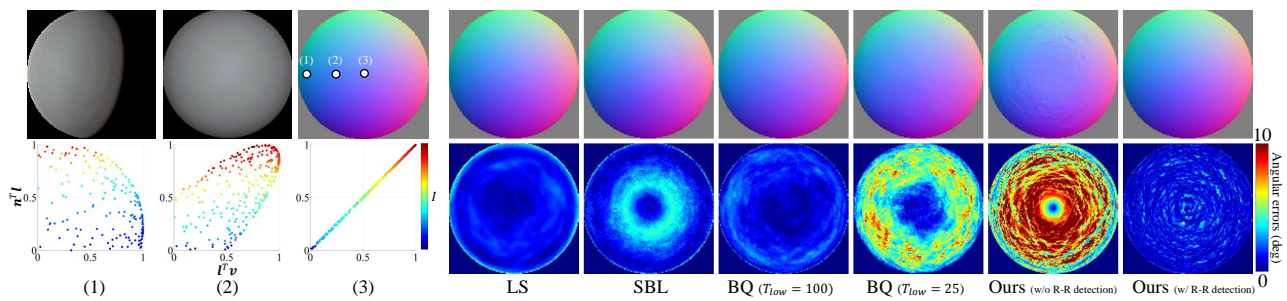


Figure 61. The results of polyethylene.

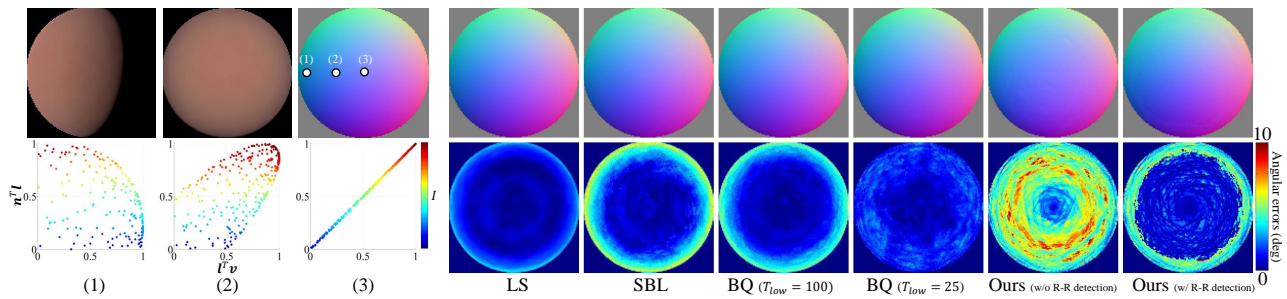


Figure 62. The results of polyurethane-foam.

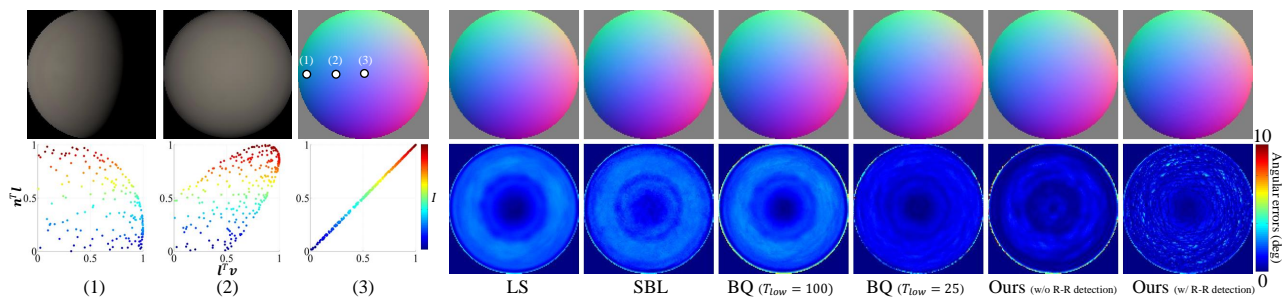


Figure 63. The results of pure-rubber.

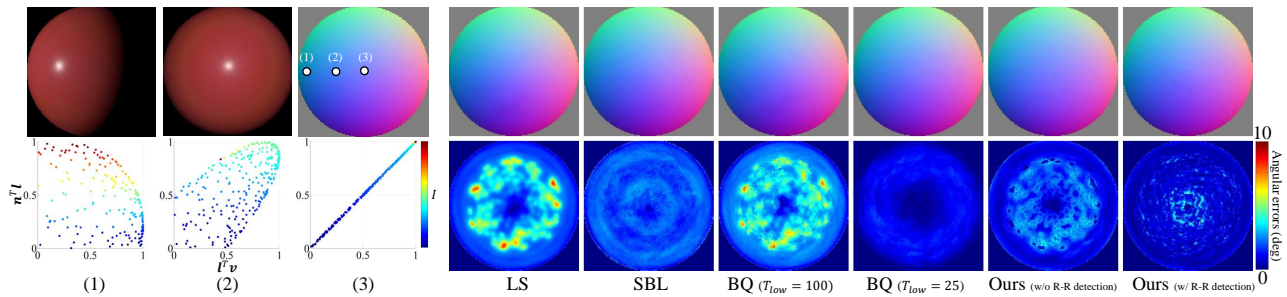


Figure 64. The results of purple-paint.

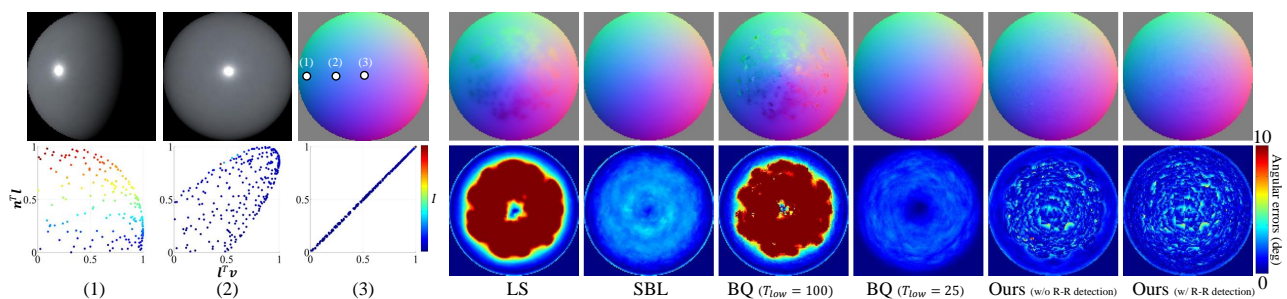


Figure 65. The results of pvc.

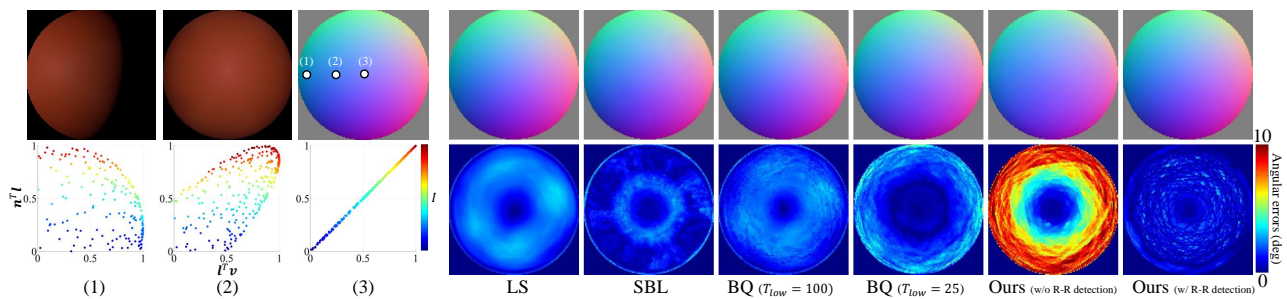


Figure 66. The results of red-fabric.

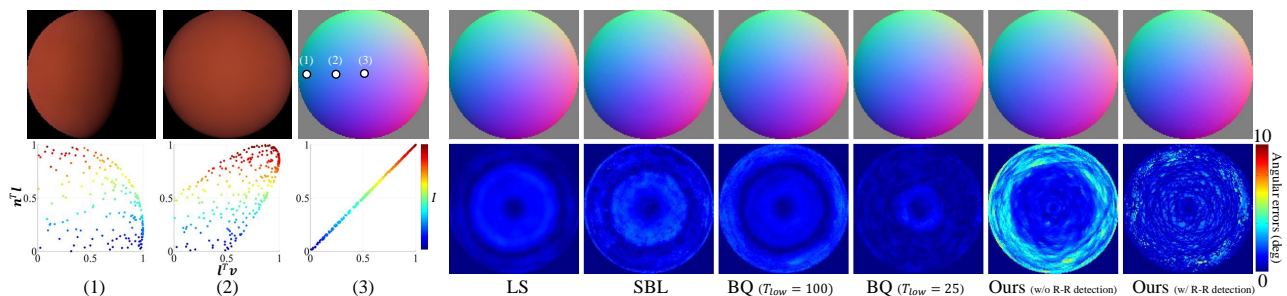


Figure 67. The results of red-fabric2.

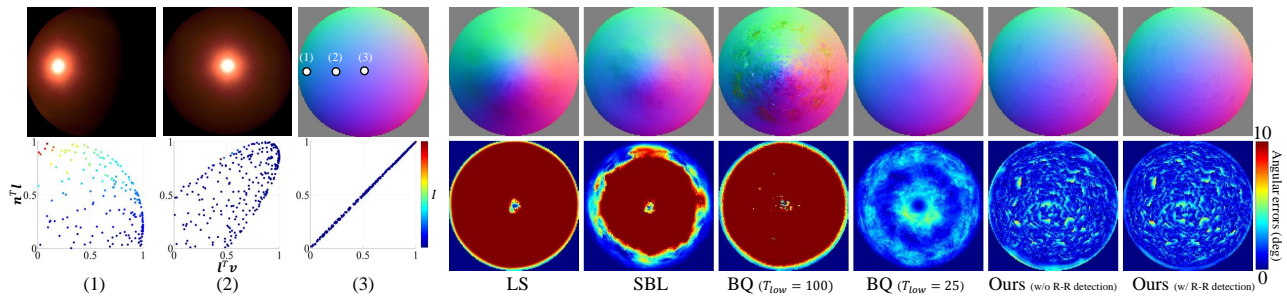


Figure 68. The results of red-metallic-paint.

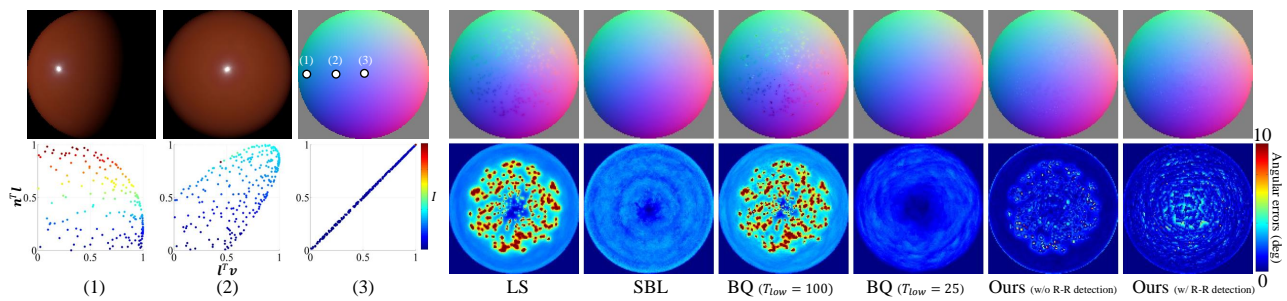


Figure 69. The results of red-phenolic.

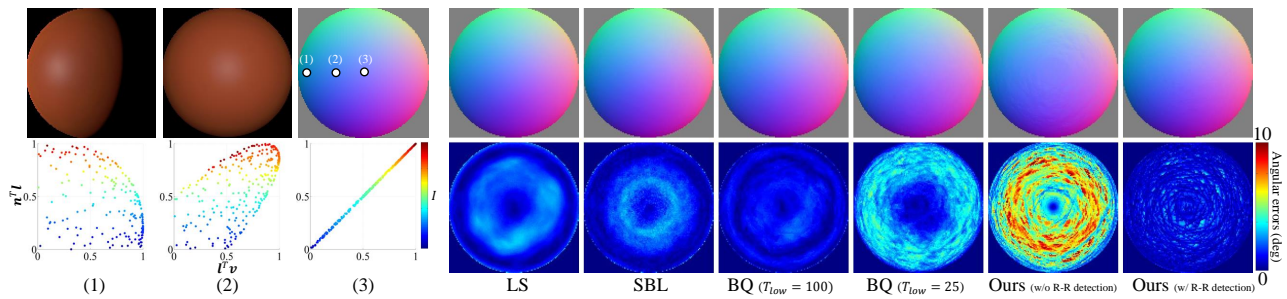


Figure 70. The results of red-plastic.

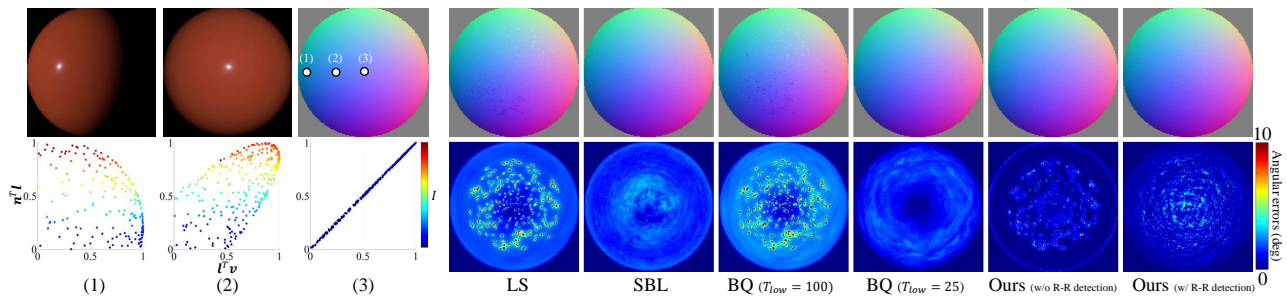


Figure 71. The results of red-specular-plastic.

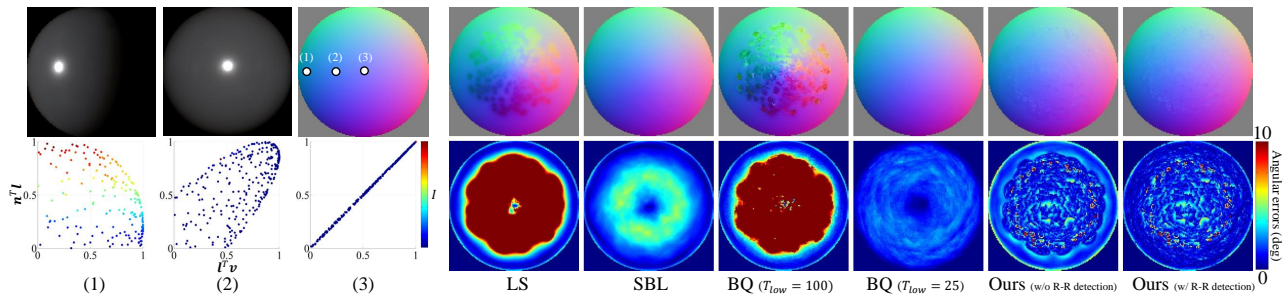


Figure 72. The results of silicon-nitride.

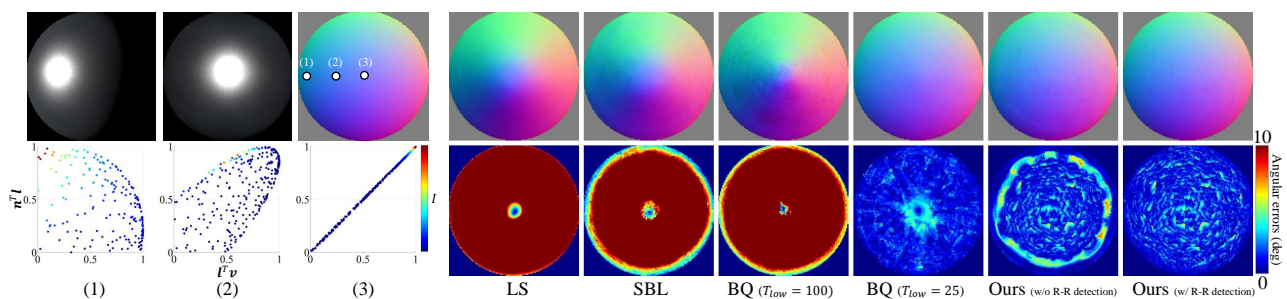


Figure 73. The results of silver-metallic-paint.

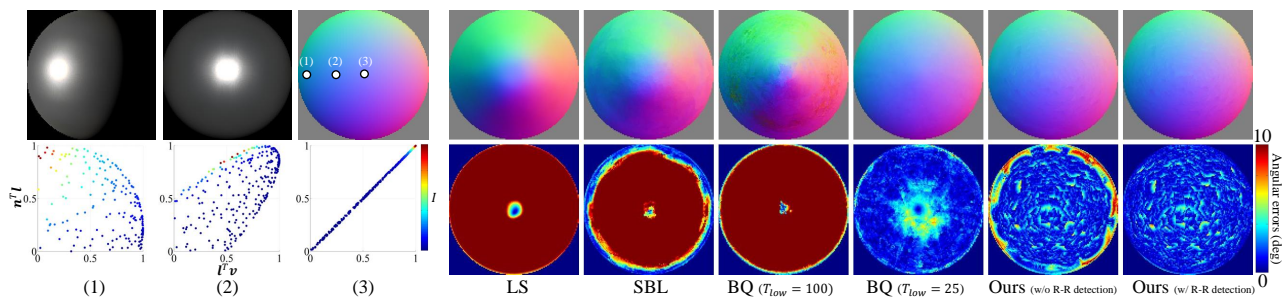


Figure 74. The results of silver-metallic-paint2.

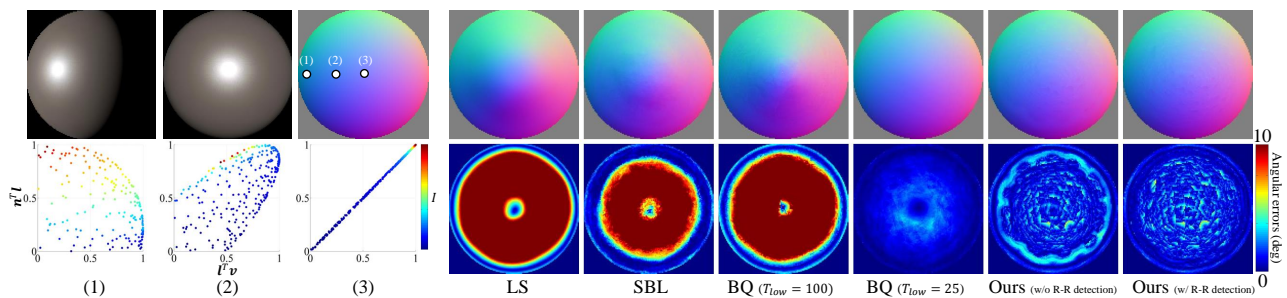


Figure 75. The results of silver-paint.

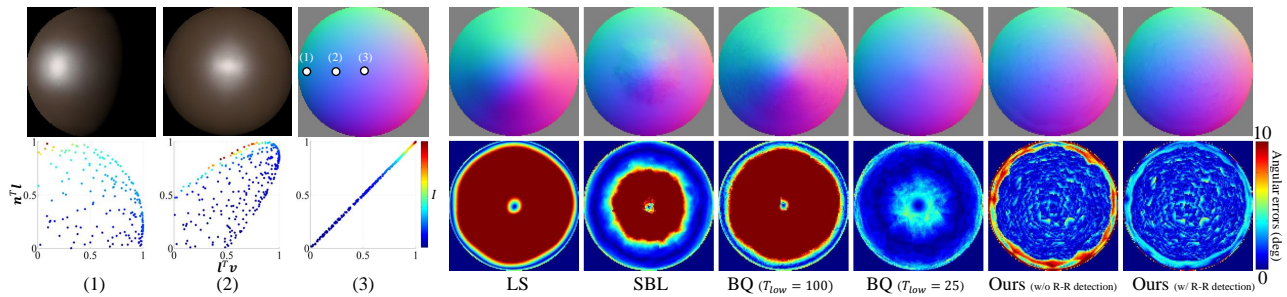


Figure 76. The results of special-walnut-224.

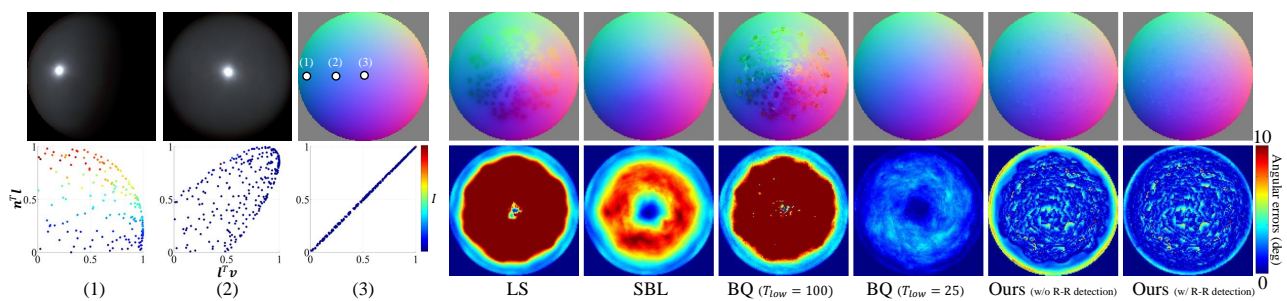


Figure 77. The results of specular-black-phenolic.

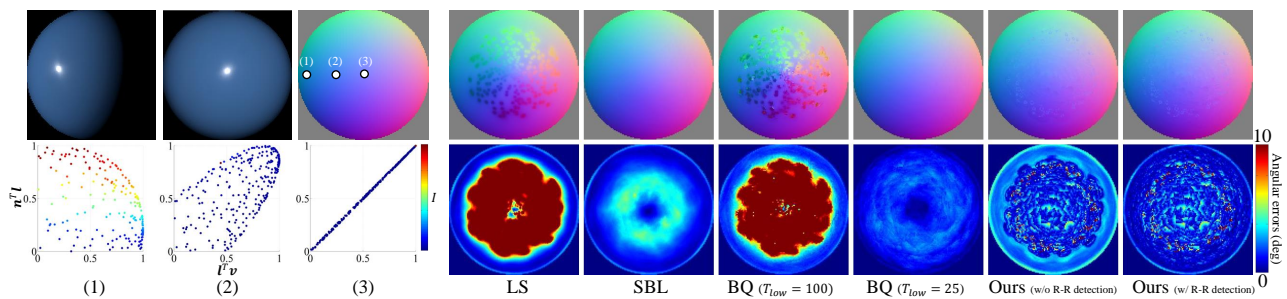


Figure 78. The results of specular-blue-phenolic.

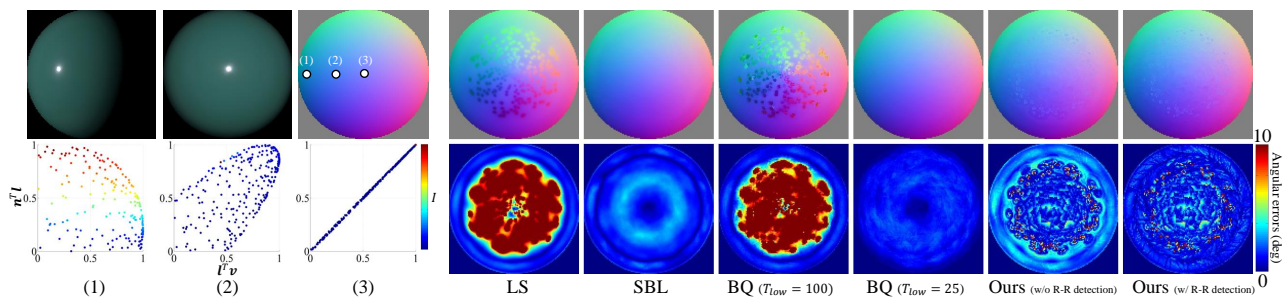


Figure 79. The results of specular-green-phenolic.

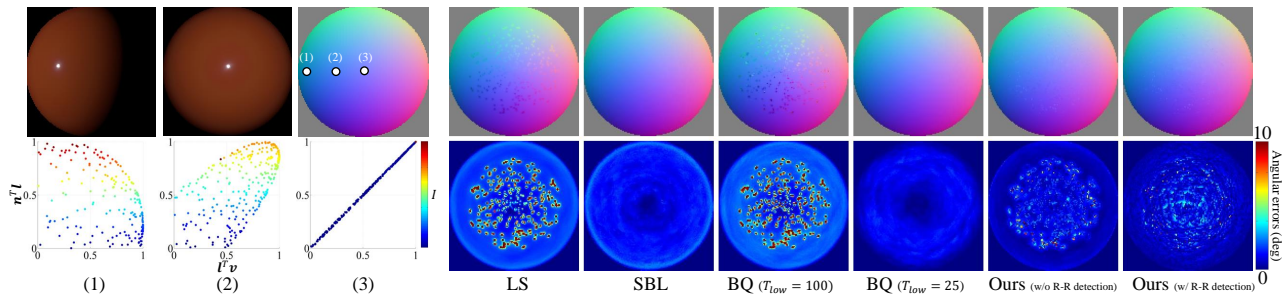


Figure 80. The results of specular-maroon-phenolic.

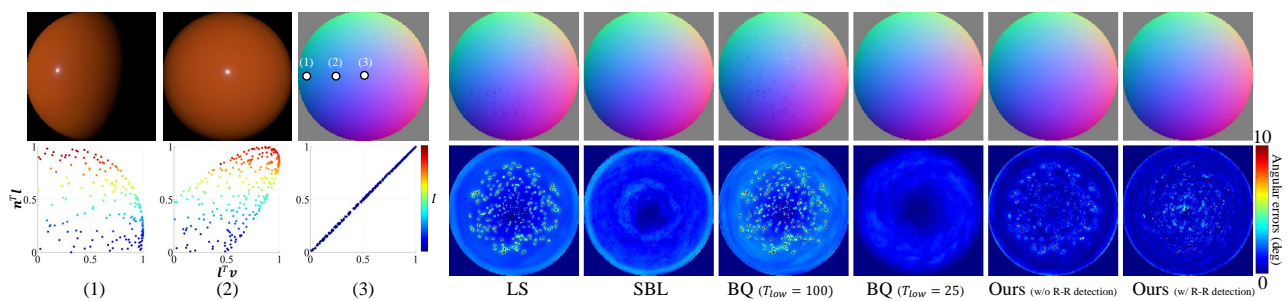


Figure 81. The results of specular-orange-phenolic.

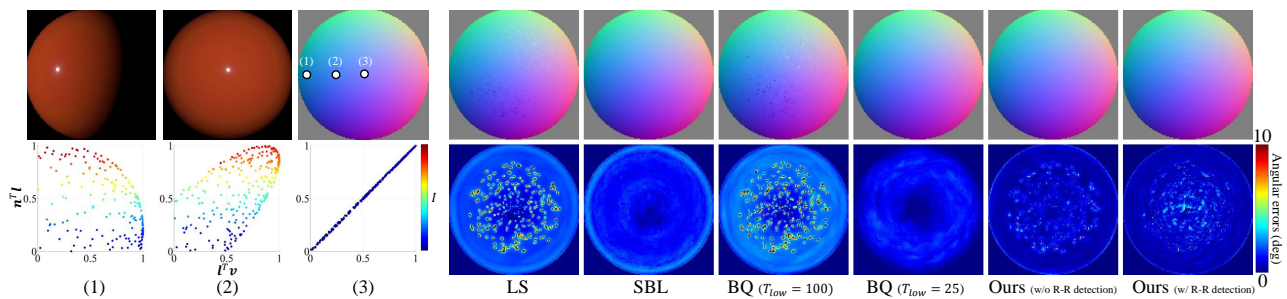


Figure 82. The results of specular-red-phenolic.

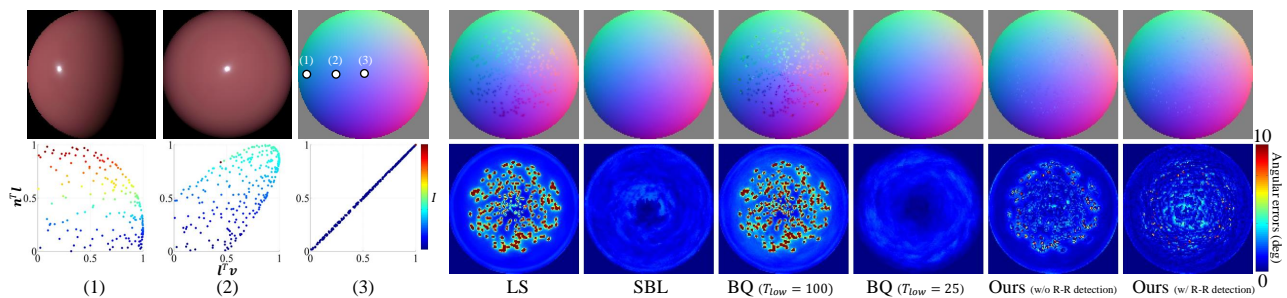


Figure 83. The results of specular-violet-phenolic.

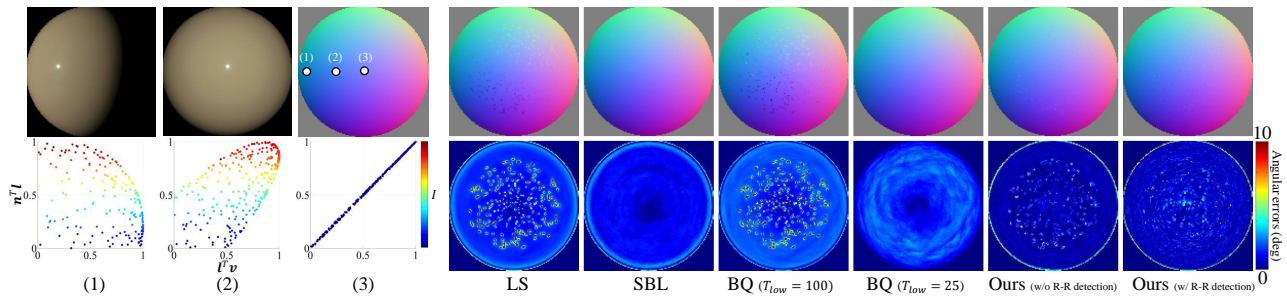


Figure 84. The results of specular-white-phenolic.

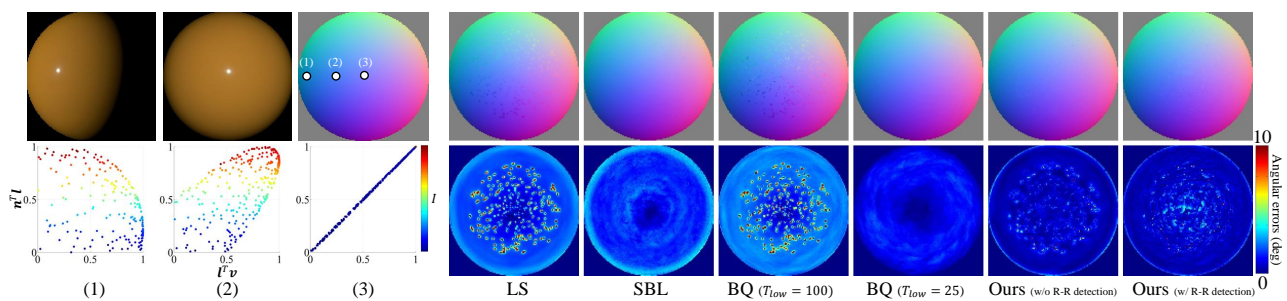


Figure 85. The results of specular-yellow-phenolic.

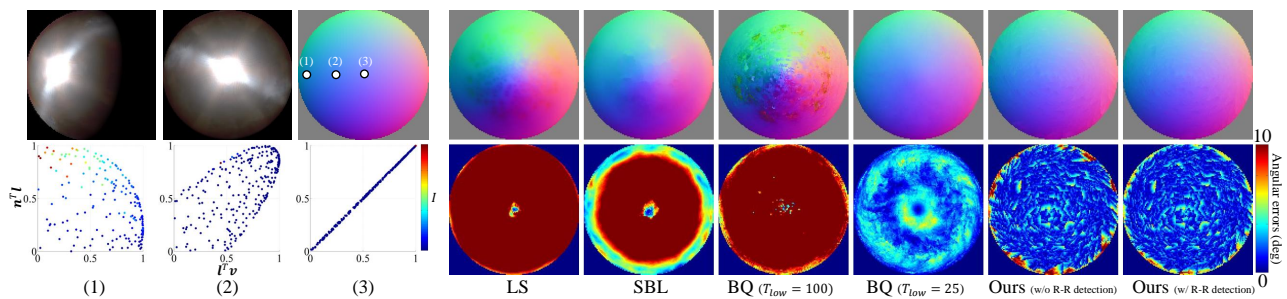


Figure 86. The results of ss440.

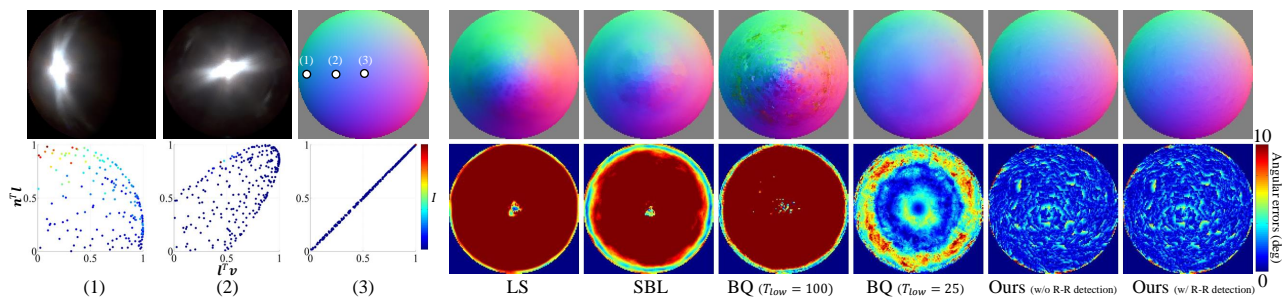


Figure 87. The results of steel.

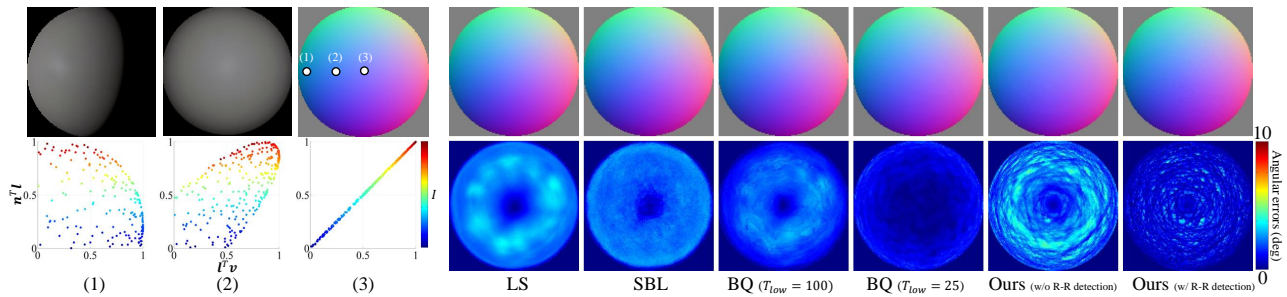


Figure 88. The results of tefflon.

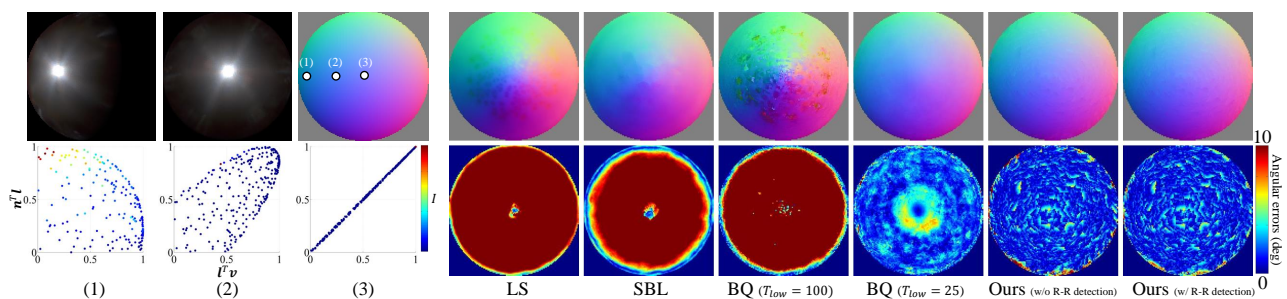


Figure 89. The results of tungsten-carbide.

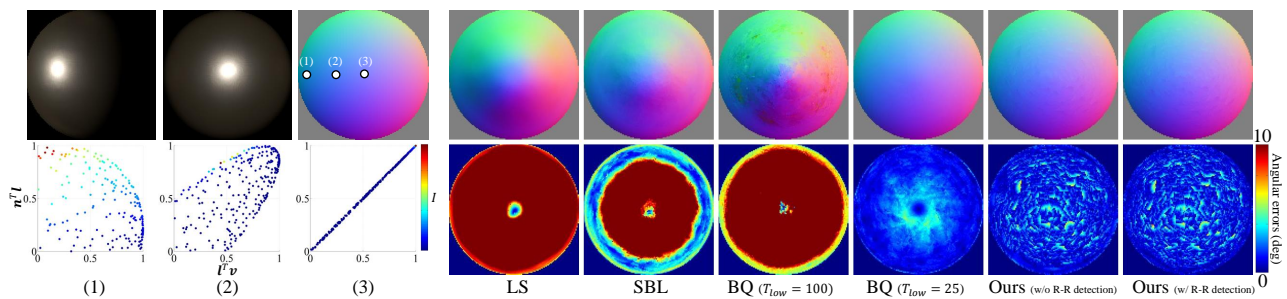


Figure 90. The results of two-layer-gold.

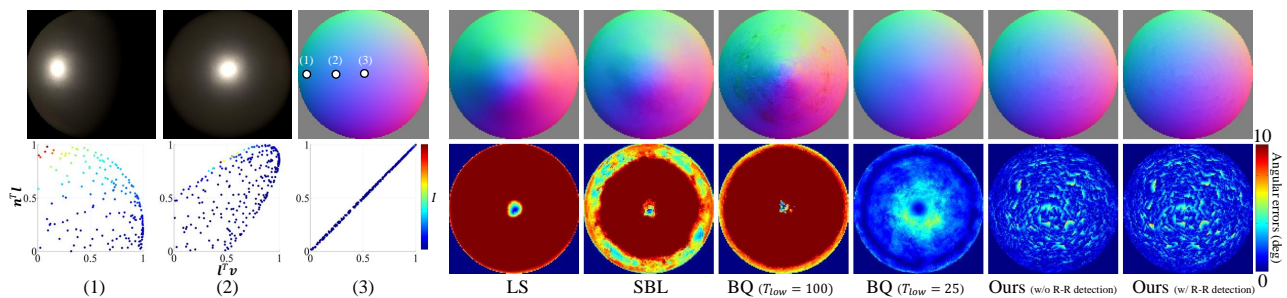


Figure 91. The results of two-layer-silver.

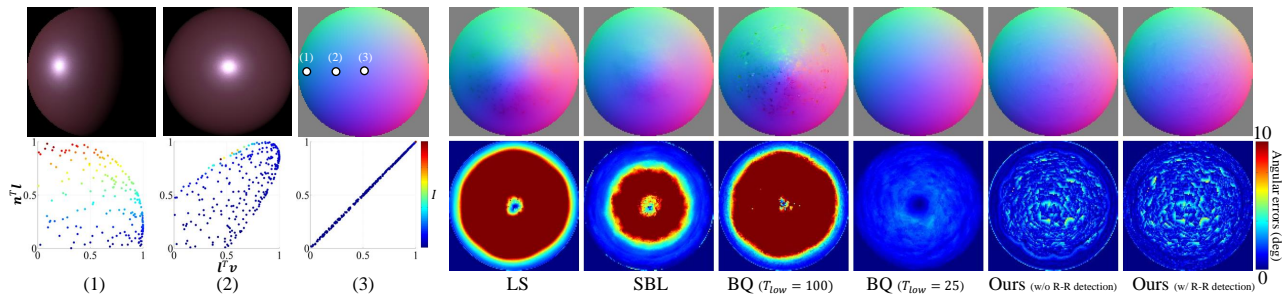


Figure 92. The results of violet-acrylic.

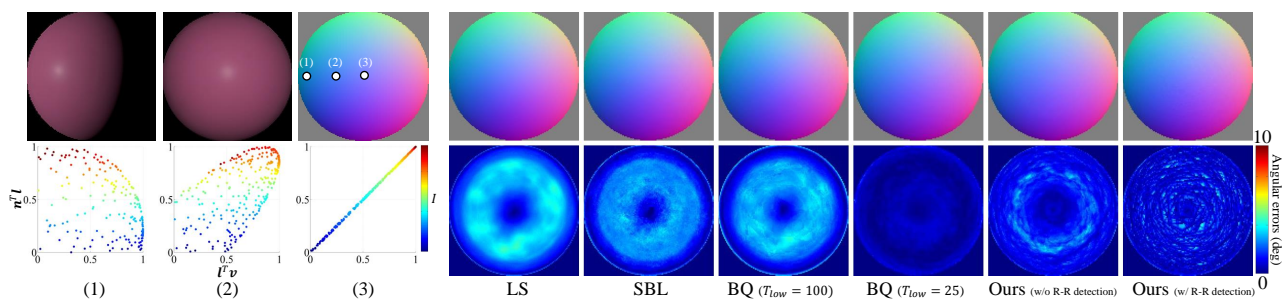


Figure 93. The results of violet-rubber.

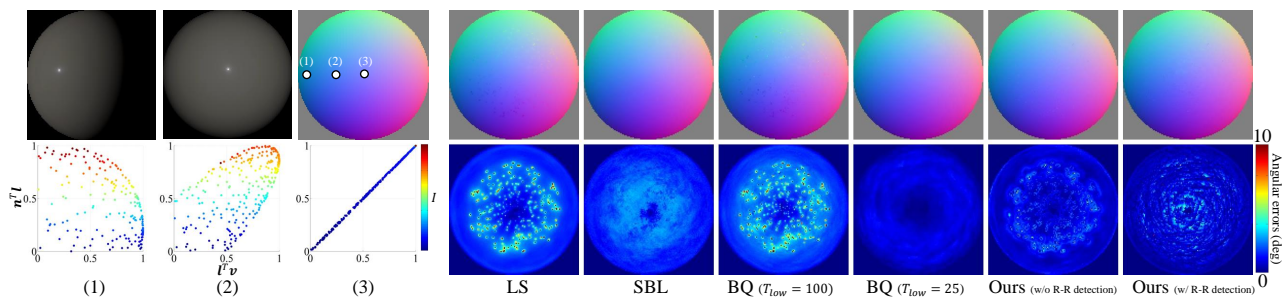


Figure 94. The results of white-acrylic.

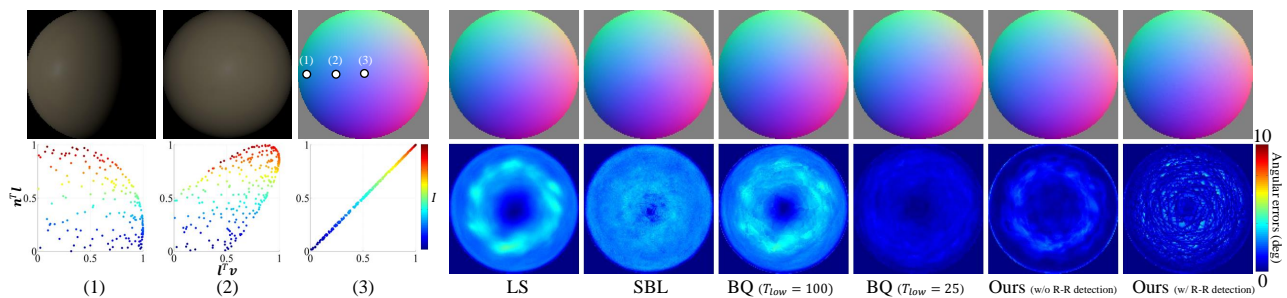


Figure 95. The results of white-diffuse-bball.

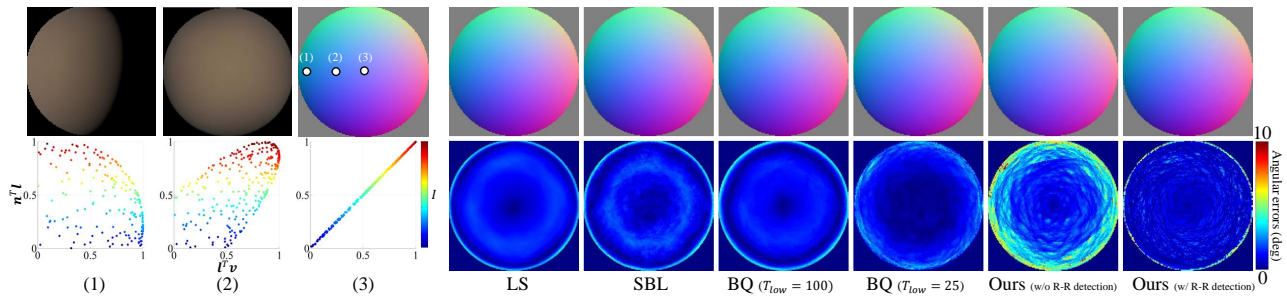


Figure 96. The results of white-fabric.

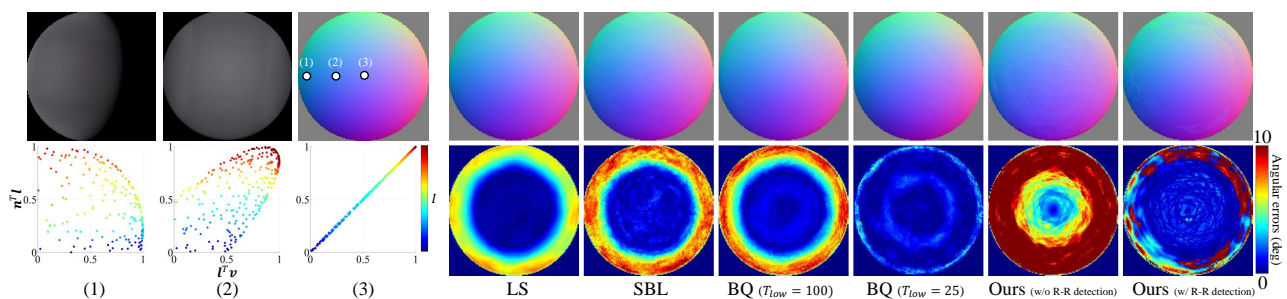


Figure 97. The results of white-fabric2.

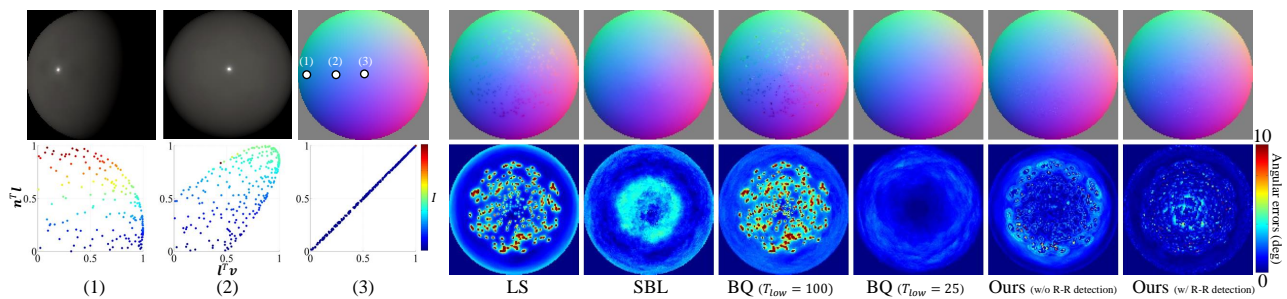


Figure 98. The results of white-marble.

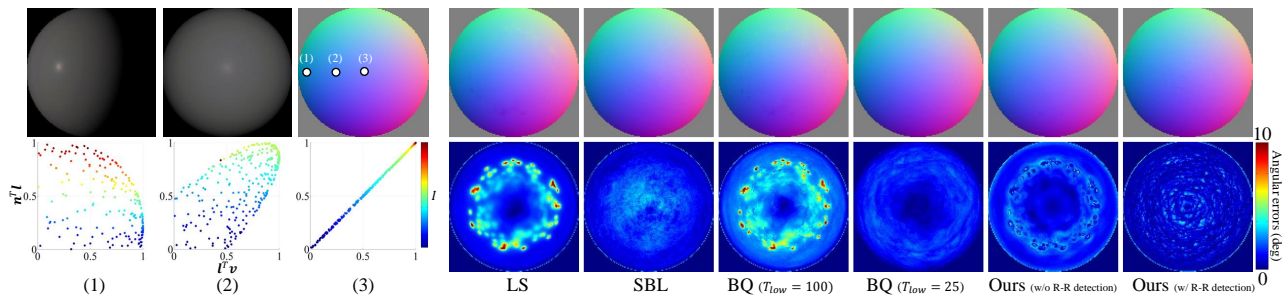


Figure 99. The results of white-paint.

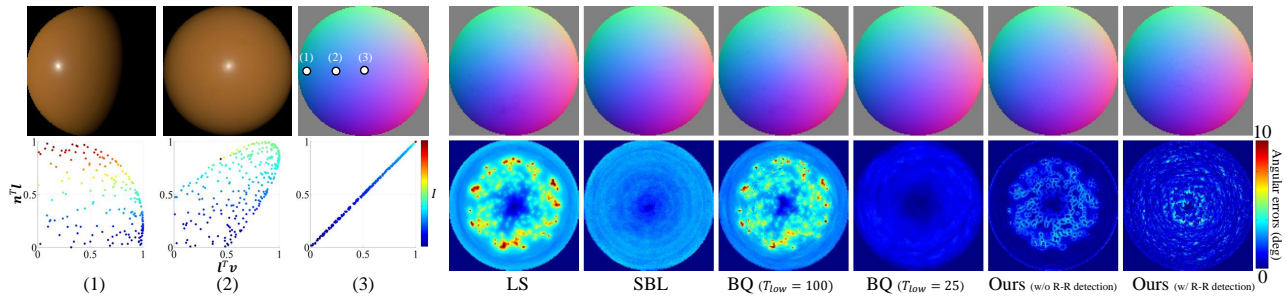


Figure 100. The results of yellow-matte-plastic.

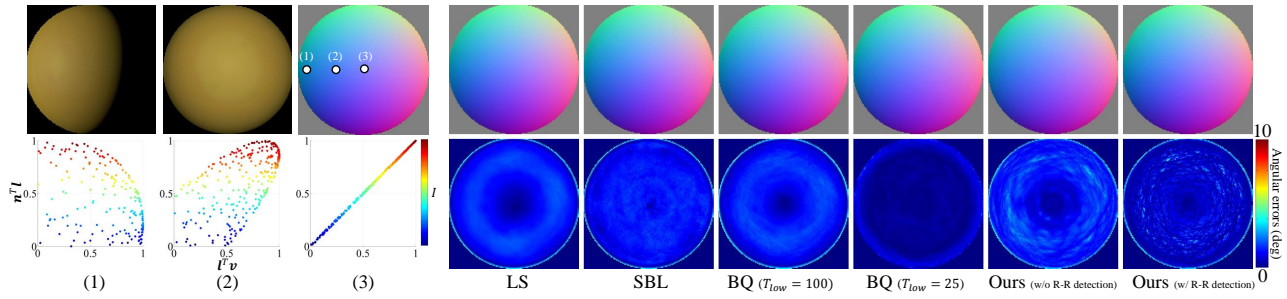


Figure 101. The results of yellow-paint.

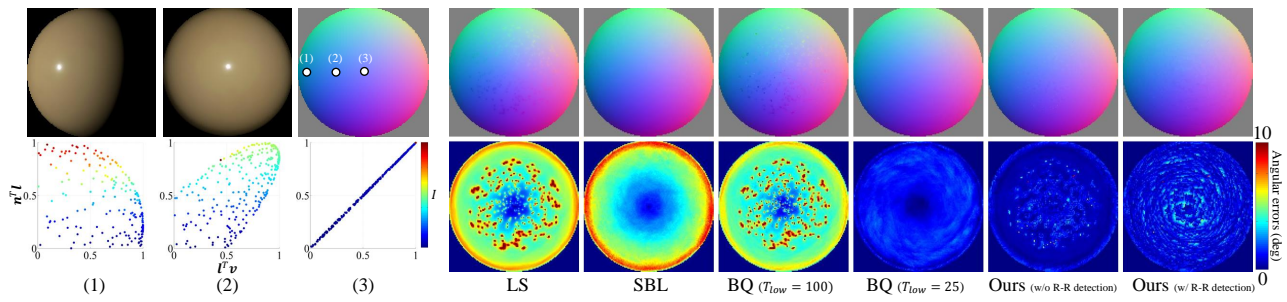


Figure 102. The results of yellow-phenolic.

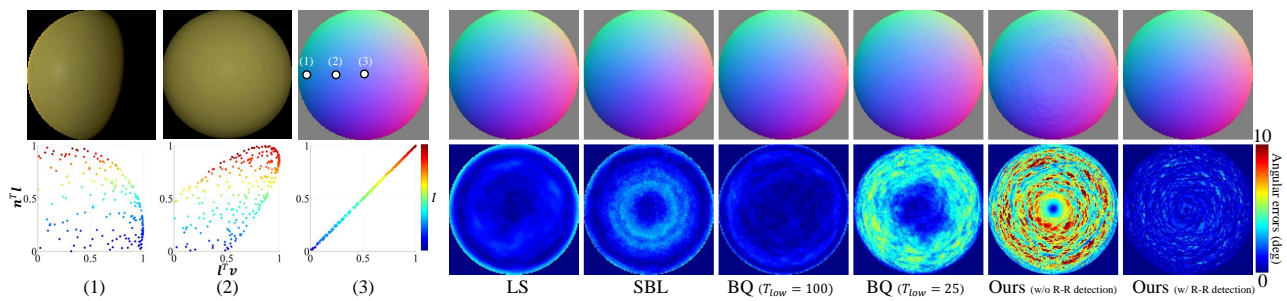


Figure 103. The results of yellow-plastic.

## References

- [1] A. Agrawal, R. Raskar, and R. Chellappa. What is the range of surface reconstructions from a gradient field ? In *Proc. ECCV*, 2006.
- [2] M. Ashikhmin and P. Shirley. An an isotropic phong brdf model. *Journal on Graphics Tools*, 5(2):25–32, 2000. 1, 4
- [3] M. Chandraker and R. Ramamoorthi. What an image reveals about material reflectance. In *Proc. ICCV*, 2011. 2

- [4] R. Cook and K. Torrance. A reflectance model for computer graphics. *ACM Trans. on Graph.*, 15(4):307–316, 1981. [1](#), [3](#), [5](#)
- [5] S. Ikehata, D. Wipf, Y. Matsushita, and K. Aizawa. Robust photometric stereo using sparse regression. In *Proc. CVPR*, 2012.
- [6] E. Lafortune, S.-C. Foo, K. Torrance, and D. Greenberg. Non-linear approximation of reflectance functions. In *Proc. ACM SIG-GRAPH*, 1997. [1](#), [4](#)
- [7] S. Lin and S. Lee. A representation of specular appearance. In *Proc. ICCV*, 1999. [4](#)
- [8] W. Matusik, H. Pfister, M. Brand, and L. McMillan. A data-driven reflectance model. *ACM Trans. on Graph.*, 22(3):759–769, 2003. [2](#), [3](#), [5](#)
- [9] R. Montes and C. Urena. An overview of brdf models. Technical report, LSI-2012-001 en Digibug Coleccion: TIC167 - Articulos, 2012. [3](#)
- [10] M. Oren and S. Nayar. Generalization of lambert’s reflectance model. In *In Proc. of the 21st annual conference on Computer graphics and interactive techniques*, 1994. [1](#), [4](#)
- [11] C. Schlick. *A fast alternative to phong’s specular model*. Eds Paul Heckbert, Academic Press, 1994. [3](#)
- [12] B. Shi, P. Tan, Y. Matsushita, and K. Ikeuchi. A biquadratic reflectance model for radiometric image analysis. In *Proc. CVPR*, 2012.
- [13] G. Ward. Measuring and modeling anisotropic reflection. *Computer Graphics*, 26(2):265–272, 1992. [1](#), [4](#)
- [14] P. Woodham. Photometric method for determining surface orientation from multiple images. *Opt. Engg.*, 19(1):139–144, 1980. [3](#), [4](#)
- [15] L. Wu, A. Ganesh, B. Shi, Y. Matsushita, Y. Wang, and Y. Ma. Robust photometric stereo via low-rank matrix completion and recovery. In *Proc. ACCV*, 2010.